Luís Manuel Farinha Bernardino de Oliveira

Bachelor degree in Science of Micro and Nanotechnologies Engineering

Quantitative nanoscopy of endosomal F-actin: Impact of an Alzheimer's risk factor

Dissertation submitted
for the attainment of the Master degree
in
Micro and Nanotechnologies Engineering

Supervisor:	Dr. Nuno Moreno, Instituto Gulbenkian Ciência
Co-Supervisor:	Dr. Rui Igreja, Assistant Professor, Faculdade de Ciências e Tecnologia, Universidade Nova de Lisboa

Examination Committee

President: Dr. Rodrigo Ferrão de Paiva Martins, Full Professor, Materials Science Department, FCT-UNL

Examiner: Dr. José Ricardo Ramos Franco Tavares, Assistant Professor, Department of Chemistry, FCT-UNL

Supervisor: Dr. Nuno Moreno, Instituto Gulbenkian Ciência

FACULDADE DE CIÊNCIAS E TECNOLOGIA
UNIVERSIDADE NOVA DE LISBOA

March, 2018

Quantitative nanoscopy of endosomal F-actin: Impact of an Alzheimer's risk factor

“If we knew what it was we were doing, it would not be called research, would it?”

Albert Einstein

Acknowledgements

É com enorme orgulho que finalmente, depois de tudo o resto, começo a escrever esta secção. A conclusão da minha tese de mestrado simboliza não só o final de uma etapa académica que culmina na obtenção do grau de mestre em Engenharia de Micro e Nanotecnologias mas também o final de uma etapa pessoal que me ajudou a crescer. Durante este percurso que se estendeu durante praticamente um ano existem inúmeras pessoas sem as quais esta etapa não teria sido tão marcante como foi.

Quero começar por agradecer ao professor Rodrigo Martins e à professora Elvira Fortunato pela criação e desenvolvimento constante do curso de Engenharia de Micro e Nanotecnologias que me proporcionou 5 anos de desafios aos quais respondi com o melhor que consegui. Tive contacto com tecnologia, equipamentos e profissionais *state of the art* que estimularam o meu interesse pela ciência e me motivaram a querer sempre alcançar mais.

Ao professor Rui Igreja por ter sido um importante elo de ligação entre o Instituto Gulbenkian Ciência (IGC) e a FCT e ter tornado possível a existência desta tese.

Em seguida quero agradecer ao meu orientador, Doutor Nuno Moreno. Enfim, para o Nuno eu sei que bastaria um obrigado e um bom passou bem porque provavelmente tem imensa coisa para fazer e todo o tempo é pouco. No entanto, não posso deixar de expor a importância que o Nuno Moreno teve durante este percurso e para a realização deste trabalho. Sem o Nuno eu não teria tido a oportunidade de ingressar IGC onde realizei grande parte do meu trabalho e onde todos os recursos foram postos à minha disposição. Para além disso foi a postura do Nuno como orientador que me fez perguntar, pesquisar e pensar sobre o meu trabalho e responder às perguntas que tive. Não só pelos *brainstorms* sobre os mais diversos temas mas também pelo profissional que é o Nuno e pela energia e genica que emana. Por isso Nuno um muito muito obrigado. Quero também agradecer ao Gabriel por me ter deixado fazer parte e ter sentido tão à vontade na Unidade de Imagiologia e Citometria do IGC durante todo o tempo em que estive a desenvolver este trabalho.

Da mesma maneira quero agradecer à minha co-orientadora, Doutora Cláudia Almeida, que me abriu as portas do seu laboratório, *Neuronal Trafficking in Ageing,* no CEDOC (Centro de Estudos de Doenças Crónicas) onde realizei tanto trabalho como no IGC. Sem a disposição da Cláudia para me receber nada disto teria sido possível. Mas ainda mais que isso foi o tempo e a grande paciência que teve comigo a explicar-me ou a pôr-me no caminho certo nas minhas grandes divagações e o acompanhamento de perto do meu trabalho que sei que não foi fácil por causa das inúmeras tarefas, compromissos e prazos que tens todos os dias. Para além disso, foi no mínimo estimulante todas as conversas que tivemos acerca das possibilidades e de tudo aquilo que podemos fazer neste laboratório. Quero-te agradecer por tudo isto e por todos os recursos que puseste à minha disposição que tornaram tudo isto possível.

Sinto-me no mínimo privilegiado por ter tido a oportunidade de trabalhar nestas duas instituições. Em ambas aprendi tanta coisa e conheci tantas pessoas que são ao mesmo tempo grandes profissionais mas também grandes companheiros. Não posso deixar de agradecer ao Nuno Pimpão pela enorme ajuda que me deu no IGC nas mais diversas ocasiões (enumerá-las ocuparia espaço que não que não tenho aqui), pelas conversas e esclarecimentos que tivemos naqueles finais de dia. À Tatiana pela enorme e incrível ajuda que me deu durante este tempo todo e sem a qual este trabalho simplesmente não tinha

acontecido, pelas boas conversas, pela paciência gigante e por todos os bons momentos durante esta etapa stressante. Ao Hugo Pereira que é um excelente companheiro de sala com quem tive muitas risadas mas também feedback. To Swadhin that allowed me to participate in his project in which I felt honored to be for a few months for the challenges it imposes to everyone involved. À Ana Vinagre que esteve comigo nas sessões de dSTORM mais engraçadas e que me mostrou o que é trabalhar bem, com ritmo e a superar desafios à partida impossíveis (selar coverslips pequenas e ainda conseguir levar ao dSTORM WHAT?!). A lista contínua e inclui o Tiago Vale, Inês Vale, o Pedro Alves, a Inês Cabral, a Marta Monteiro, a Mariana Fernandes, a Catarina Perdigão, a Farzaneh Mirfakhar, o Luís Marcelo. Todos estiveram presentes de diversas formas ao longo deste percurso.

Aos meus grandes amigos e companheiros de curso Viorel, Alexandre, Tiago, Coroa, Crespo, Inês, Ana Beaumont, Daniela, David, Marco, João Luís, Shiv, Alexandra, Emma, Cátia, Vasco com os quais passei experiências para a vida e que me acompanharam ao longo destes 5 anos na FCT.

A todos os meus amigos para além da faculdade que me ajudaram a espairecer e a esquecer a tese durante tantos e diversos programas. Sem isso seria muito difícil manter a motivação e a energia para continuar este projecto.

Por fim, uma grande palavra de carinho aos meus pais e ao meu irmão que durante este tempo sempre se mostraram interessados naquilo que estava a fazer, me viram a stressar bastante, me acalmaram mas também por me darem aquele impulso final quando diziam “Já não devias ter acabado isso?”.

A vida é feita pelos nossos alcances mas também pelas pessoas que nos rodeiam.

Um bem haja a todos!

Abstract

dSTORM is a super resolution technique capable of breaking the diffraction limit present in conventional light microscopy. As a molecular imaging technique it gives access to a new kind of data that other super resolution techniques cannot. Some relevant findings were a) identification of nuclear pore proteins symmetry, b) protein distribution inside clusters at the plasma membrane c) organization between proteins in axons. Alzheimer's disease is the most frequent dementia and one of the biggest problems in our aged society. Genomic studies identified variants in the gene CD2AP associated with the disease. Recent studies showed that CD2AP silencing traps the amyloid precursor protein in early endosomes, increasing the production of beta-amyloid: the Alzheimer's disease hallmark toxic protein. It is unclear, however, the link of CD2AP as actin cytoskeleton regulator and therefore the link of F-actin on the CD2AP dependent beta-amyloid production. Preliminary results using conventional light microscopy showed less perinuclear F-actin puncta upon CD2AP silencing. We aimed to merge cell biology and super-resolution microscopy to study F-actin patterns with nanometric precision in the perinuclear region and their relationship with endosomes. By accessing individual molecules, their location and by implementing quantification analysis we found F-actin more proximal to early endosomes than late endosomes, suggesting an early role for F-actin during endosomal sorting and maturation. Importantly, CD2AP silencing and overexpression of wild-type and of an Alzheimer's mutant form, altered the quantity of F-actin in the perinuclear region, its clustering ability and association with early endosomes. Our results indicate that F-actin regulation has a role in the CD2AP-dependent mechanism of beta-amyloid production in early endosomes, thus contributing to the development of Alzheimer's disease.

Keywords: Alzheimer, CD2AP, dSTORM, Actin, Intracellular Traficking, Point Pattern Analysis

Resumo

dSTORM é uma técnica de super resolução que permite ultrapassar o limite imposto pela difração da luz presente em microscopia óptica convencional. Como técnica de microscopia molecular fornece novos tipos de informação que outras técnicas da super resolução não fornecem. Entre algumas descobertas relevantes tem-se: a) identificação de simetrias em proteínas do poro nuclear, b) distribuição de proteínas em aglomerados na membrana celular, c) organização entre proteínas em axónios. Alzheimer é o caso de demência mais frequente e um dos maiores problemas da nossa sociedade envelhecida. Estudos genómicos identificaram variantes no gene CD2AP associadas com a doença. Estudos recentes mostraram que ao remover CD2AP, um conhecido regulador de actina, a proteína percursora de amiloide beta é retida na membrana de endossomas precoces, aumentando a produção de beta amiloide, a proteína distinta da doença de Alzheimer. No entanto é pouco claro se a actina tem um papel na produção de beta-amiloide dependente de CD2AP. Resultados preliminares baseados em microscopia óptica convencional mostram menos quantidades de actina filamentosa na zona adjacente ao núcleo, na ausência de CD2AP. O nosso objectivo foi juntar a biologia celular com microscopia de super resolução para estudar os padrões de actina na região adjacente ao núcleo com precisão nanométrica e a sua relação com os endossomas. Acedendo a cada molécula, à sua localização e implementando análises de quantificação, acabámos por observar que a actina filamentosa presente nesta região tem uma maior proximidade com os endossomas precoces comparando com endossomas tardios, sugerindo um papel primário durante a maturação e distribuição da carga dos endossomas. Ao remover e ao sobre expressar uma forma normal e uma forma mutante de CD2AP também foi observada uma alteração na quantidade de actina filamentosa nesta região, bem como na sua capacidade de agregação e na relação com os endossomas precoces. Em suma, os nossos resultados indicam que a regulação de actina está implicada nos mecanismos de produção de beta amiloide nos endossomas precoces, que podem contribuir para o desenvolvimento de Alzheimer.

Palavras-chave: Alzheimer, CD2AP, dSTORM, Actina, Tráfico Intracelular, Análise Espacial de Pontos

Table of Contents

List of Figures

List of Tables

Abbreviations and Symbols

βCTF	β Carboxyl Terminal Fragments
Da	Dalton
µm	micrometer
µl	microliter
mM	mili-Molar
nm	Nanometer
Aβ	Amyloid Beta
ABP	Actin Binding Protein
AD	Alzheimer's disease
ADP	Adenosine Diphosphate
APOE	Apolipoprotein E
Arp 2/3	Actin-related proteins 2/3
APP	Amyloid Precursor Protein
ATP	Adenosine Triphosphate
BACE1	Beta-site APP Cleavage Enzyme 1
CD2AP	CD2-associated protein
CHO	Chinese Hamster Ovary
CP	Capping Protein
DBSCAN	Density-Based Spatial Clustering of Applications with Noise
DNA	Deoxyribonucleic acid
dSTORM	direct-Stochastic Optical Reconstruction Microscopy
EEA1	Early Endosome Antigen 1
EGF	Epidermal Growth Factor
EMCCD	Electron Multiplying Charge-Coupled Device
EOAD	Early-onset Alzheimer's disease
ER	Endoplasmatic Reticulum
ESCRT	Endosomal Sorting Complexes Required for Transport
F-actin	Filamentous-actin
FOV	Field of View
G-actin	Globular Actin
GFP	Green Fluorescent Protein
GWAS	Genome Wide Association Study
Hrs	Hepatocyte growth factor-regulated tyrosine kinase substrate
ILV	Intra luminal Vesicles
LAMP1	Lysosomal-associated membrane protein 1
LOAD	Late-onset Alzheimer's disease
MVB	Multi-Vesicular Bodies
NFT	Neurofibrillary tangles

NPF	Nucleation Promotion Factor
N-WASP	Neural Wiskott - Aldrich syndrome Protein
PDGF	Platelet Derived Growth Factor
PM	Plasma Membrane
PSEN1	Presenilin 1
PSEN2	Presenilin 2
PSF	Point Spread Function
ROI	Region of Interest
sAPPα	Amyloid Precursor Protein (soluble α-cleaved fragment)
sCMOS	Scientific Complementary Metal Oxide Semiconductor
SH3	Src Homology 3 domain
SMLM	Single Molecule Localization Microscopy
SNP	Single Nucleotide Polymorphism
SNR	Signal to Noise Ratio
VEGF	Vascular Endothelial Growth Factor

1. Introduction

1.1 Contextualization and Pathophysiology of Alzheimer's Disease

Alzheimer's disease (AD) is one of the most common neurodegenerative disorders responsible for 60 % to 80 % of dementia cases. The hallmarks of the disease are the accumulation of amyloid-β (Aβ) plaques, originating from the Amyloid precursor protein (APP), outside the neurons and of hyperphosphorylated tau neurofibrillary tangles (NFT's) inside neurons both ending in damage and eventual death of neurons [1,2]. There are two forms of the disease: Early-Onset Alzheimer's Disease (EOAD) and Late-Onset Alzheimer's Disease (LOAD). EOAD happens in people under 65 years-old and is only responsible for 1 % to 6 % of the cases and it is potentiated by mutations in three genes involved in the generation of Aβ: APP, Presenilin 1 (PSEN1) and Presenilin 2 (PSEN2). LOAD, the most common, happens after 65 years old. Here the major risk factors are: environmental, ageing and the inheritance of the E4 polymorphism in *APOE* gene [1,3,4]. The APOE-E4 is the most significant genetic risk factor and was replicated in multiple DNA sequences from across the human genome to identify common gene alterations in AD (Genome Wide-Association Study - GWAS) [5–7]. Meta-analysis of several GWAS ranked these genes and CD2AP is among the top ten risk factors for AD, a gene involved in endocytosis and regulation of the actin cytoskeleton, both critical for the normal processing cascade of APP [8–10].

1.2 CD2AP and Intracellular Trafficking

CD2AP is a multifunctional adapter type molecule localized in the cytoplasm, membrane ruffles and leading edges of cells. It has a molecular weight of approximately 70 kDa, three SH3 domains in the N terminus, a proline-rich region containing and a coiled-coil domain at the C terminus of the protein. SH3 domains are found in molecules related to signaling and cytoskeleton [11] (**Figure 1.1**).

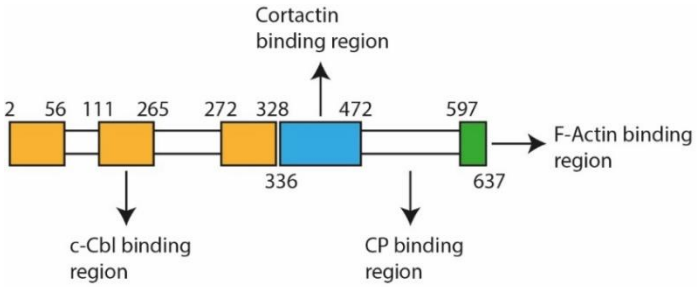

Figure 1.1 - Schematic of CD2AP protein. Numbers indicate the limits of each domain. Orange indicates SH3 domains: Src homology 3 domain where the second one links to the c-Cbl protooncogene [12]. Blue indicates the proline rich domain that interacts with the Sh3 domain of cortactin [13,14]. Green is the coiled coil domain with an F-actin binding site[15]. Between proline rich and coiled coil domain there is capping protein binding site [14,16]. Adapted from [12].

The name CD2AP (CD2 – associated protein) comes from being first identified as a scaffold protein necessary for clustering CD2 and polarizing the actin cytoskeleton at the immunological synapse, that is, the interface between a T lymphocyte and an antigen-presenting cell [11]. In other studies, CD2AP colocalized with cortactin, a protein involved in polymerization of F-actin, through interaction with the Arp2/3 complex. Direct interaction between the two molecules has been mapped to the proline rich region of CD2AP [13,14]. Moreover, CD2AP is known to interact as well with capping protein (CP) [14,16], another regulator of F-actin

assembly. This strong connection with molecules related with actin could link CD2AP and actin in several mechanisms of vesicular trafficking. In addition, actin and CD2AP, were shown to colocalize when associated to MVBs (Multi-Vesicular Bodies) belonging to late endosomal compartments [17] and to control dynamic F-actin structures in early endosomes necessary to transfer VacA to late endosomes [18]. These findings indicate that CD2AP could be necessary to sort protein into the degradative pathway (like APP) and this is corroborated by the fact that the formation of MVBs is required to downregulating activated signaling receptors and that CD2AP has been involved in EGF receptor trafficking[13], PDGF receptor [12] and in VEGF receptor degradation[19].

1.3 F-Actin and Intracellular Trafficking

Actin is the most abundant protein in most eukaryotic cells, it participates in more protein to protein interactions than any other protein and it is an essential component of the cytoskeleton. The actin cytoskeleton functions in the generation and maintenance of cell morphology and polarity, endocytosis and intracellular trafficking and in motor functions like contraction, cell division and motility. The monomeric form, G-Actin interacts with other actin monomers, transforming the monomeric form in a polymerized or filamentous form called F-actin [20,21].

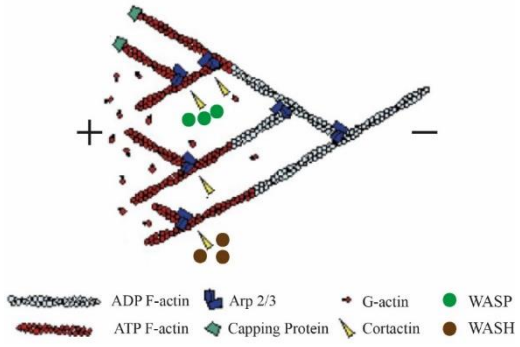

Figure 1.2 - Actin treadmilling scheme and associated Actin Binding Proteins (ABPs). The barbed end (+) is the polymerization site where new monomers are added and the minus end (-) is the depolymerization site [22]. The Arp 2/3 complex promotes nucleation and branching activity [21,23,24]. Cortactin stimulates a new conformation of the "mother" branch by interacting with F-actin and mediates Arp 2/3 and WASP/WASH recruitment [25–27]. Capping protein binds to the barbed-end (+) blocking the addition or loss of actin subunits [14,16,28]. Adapted from [24].

The resultant filaments are polarized (plus and minus end). The addition of monomers is made on both ends but the plus end grows faster than the minus end. Monomers to be added carry ATP which can be hydrolyzed and converted to ADP (more instable), making easier to dissociate at the minus end, in a mechanism known as actin filament treadmilling [20–22,29]. This is a dynamic process mediated by a large pool of proteins called Actin Binding Proteins (ABPs) (**Figure 1.2**).

Endocytosis is required to recycle plasma membrane lipids, traffic proteins and for uptake or downregulation of cell surface receptors or proteins. Actin is present in the formation of clathrin coated endocytic vesicles, the most common endocytosis mechanism, in a polymerization process dependent of others ABPs like Arp2/3 complex, N-WASP and cortactin [30–32]. Here actin is thought to provide the pressure necessary to invaginate the membrane [33–35]. Preventing actin polymerization was shown to alter vesicle

formation and its separation from the plasma membrane [31,33]. A similar mechanism might happen after vesicle fusion with early endosomes where the transported cargo can be sorted into tubular extensions, being recycled to the plasma membrane, or incorporated in endosomal intraluminal vesicles (ILVs) and follow to the degradative pathway [36,37]. The recycling route is Arp2/3 and WASH dependent. These two proteins both stimulate the development of F-actin networks at the tubular extensions to help separating them from endosomes [38]. Upon WASH knockdown, endosomes were reported to form exaggerated tubules or no tubules at all, indicating that the branched F-actin networks are crucial for cargo exiting [38,39].

Cargo for degradation depends on sorting signals. Ubiquitin is one of the responsible signals working through covalent attachment to cellular proteins. It changes the stability, localization, or activity of the target protein [40]. Recognition of ubiquitinated proteins is made by the hepatocyte growth factor-regulated tyrosine kinase substrate (Hrs) [41]. Hrs also binds to clathrin, present in early endosomes exclusively involved in sorting cargo to the degradative pathway. The binding of Hrs to ubiquitin and clathrin leads to the formation of sorting microdomains that take the cargo into ILVs, separating the two types of cargo: recycled and for degradation [41,42]. Endosomal clathrin was reported to stimulate polymerization of F-actin at the immunological synapse [43] and a similar mechanism could evolve actin polymerization in ILV formation.

1.4 F-Actin, CD2AP and Aβ

APP is a transmembrane protein with large extracellular domains. Its precise function remains unknown but several studies have shown that APP is necessary for the normal cell growth, motility, neurite outgrowth and survivability [44]. The protein has several processing pathways and some lead to the generation of Aβ. After being synthesized in the endoplasmatic reticulum (ER) APP is carried to the TGN following the secretory pathway to the plasma membrane [45–47]. At the plasma membrane, APP is either cleaved by α-secretase to produce a soluble domain of APP called sAPPα (soluble APP) which is neuroprotective, or it is endocytosed [48,49]. Upon entering endosomes, cleavage by β-secretase can occur, being the most important one BACE 1, crucial for cleavage of APP at the N-terminal β controlling the rate of generation of Aβ [50,51]. After this, the resultant domain of APP (known as β Carboxyl Terminal Fragments – βCTF) is cleaved by γ-secretase, producing p83 and two main forms (depending on the cleavage site) of Aβ: Aβ 40 and Aβ 42, being the last the most neurotoxic [52]. Both BACE 1 and γ-secretase are found in endosomes. In normal cells the Aβ generation is kept to a minimum [53–57] since BACE 1 recycled back to the plasma membrane (through fission processes and recycling endosomes) [55,58] and APP is marked for degradation and incorporated in ILVs of the endosome and to follow the degradative pathway until the lysosomes (**Figure 1.3 a**)[58,59].

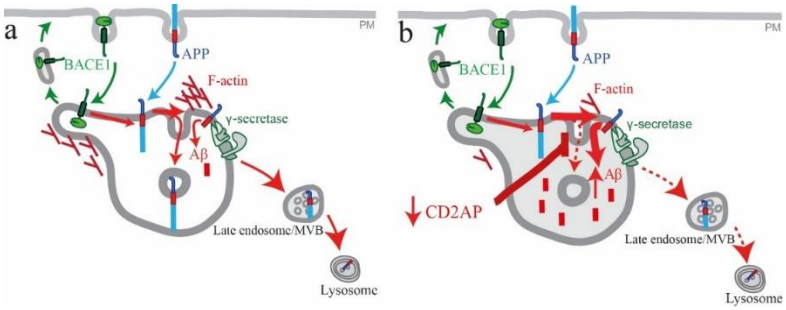

Figure 1.3 - Model for the role of CD2AP in Aβ endocytic generation in neuronal cells. **a)** Normal early/sorting endosome. In the presence of CD2AP endosomal F-actin is present at normal levels and regulates sorting mechanisms. APP is normally processed and Aβ levels are kept to a minimum. Some APP is cleaved by BACE1 and γ-secretase. The major part is sorted for degradation through the degradation pathway. **b)** Alzheimer's early/sorting endosome. Absence of CD2AP keeps unusual quantities of APP at the membrane where it is cleaved and increasing endosomal Aβ levels. Sorting for degradation is affected since most of APP was already cleaved, originating Aβ. F-actin levels also decrease and this could be in the origin of deficient sorting mechanisms for degradation. Adapted from [60].

In a recent study, *Ubelmann et al* [60] showed that CD2AP knock down increased Aβ levels through trapping of APP at the early endosome membrane and thus increasing meeting chances between APP and BACE1. It was also observed, in results yet to be published, that in the in the absence of CD2AP that bright puncta of F-actin visualized through conventional fluorescence microscopy in the perinuclear region suffer a great decrease in its intensity (**Figure 1.3 b**). These data suggest a potential role for F-actin dynamics in the CD2AP-dependent sorting of APP for degradation. CD2AP could be controlling actin polymerization and thus control APP sorting or the membrane invagination process required for ILV formation.

1.5 Super Resolution Microscopy and dSTORM

For many years the most used technique to understand biological processes was fluorescence light microscopy [61]. However, the resolution was diffraction limited due to the wave nature of the light when passing through the objective of a microscope. Both Ernst Abbe and Rayleigh described it, differing only in the criteria of when two objects are distinguishable from each other [62] (**Figure 1.4 a**).

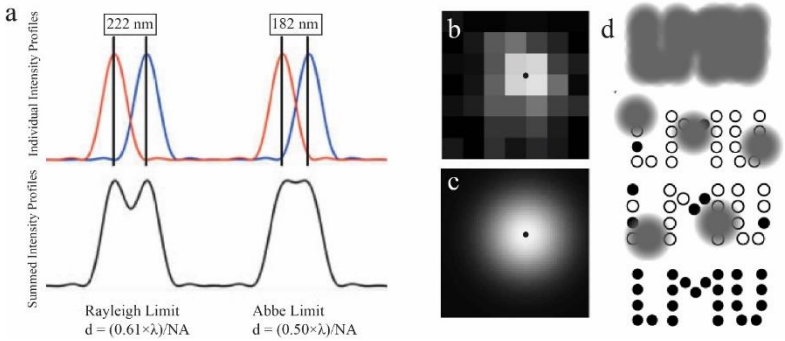

Figure 1.4 - Conventional resolution limits and SMLM dSTORM protocol. **a)** Different resolution criteria. Both assuming 510 nm emission wavelength and a 1.4 objective numerical aperture. **On top** the individual emitter intensity profiles of the PSF's (Point Spread Function). **On bottom** the profile of merged PSF's. **b)** Raw image of a PSF. **c)** Fitting a Gaussian model to b). The black dot indicates the calculated center of the emitter. **d)** SMLM dSTORM localization protocol. **From top to bottom: Top)** An array of diffraction limit and indistinguishable PSF's. **Middle)** After inducing the initial dark state, the stochastic nature of dSTORM stochastically activates fluorophores in a transient process. **Bottom)** The set of PSF's is well resolved through determination of each center by the procedures of b) and c), resulting in higher resolution. Adapted from [63,64].

In order to watch biological processes at protein levels led to the creation of super resolution techniques. One of these techniques is dSTORM and it belongs to the group known as Single Molecule Localization Microscopy (SMLM) [65] because it detects the emitter center individually.

The response of a microscope to a point of light is described by a model known as the Point Spread Function (PSF) that reflects the intensity distribution of the light coming from the emitting source [62,65–68]. Illuminating a labeled structure results in an array of several PSFs making impossible to distinguish individual point sources within the same diffraction limited area due to the merging of their PSFs [67], **Figure 1.4 d-Top**. dSTORM enables the presence of only one emitter present at this area at a time by using a combination of reversibly switchable probes like Alexa-647 and specific imaging mediums to induce fluorophore switching between a bright (ON) and dark (OFF) state, **Figure 1.4 d-Middle**, and fulfilling the requirements necessary to achieve the higher precision possible [69]. These requirements are: a) Emitting a high number of photons and b) Low ON_{state}/OFF_{state} ratio (Duty Cycle). High photon count per molecule improves the Signal to Noise Ratio (SNR) and it's a prime parameter to calculate with accuracy the position of the molecule (**equation 1.1**), **Figure 1.4 d-Bottom**. A low duty cycle lowers the probability of having more than one molecule in the ON state in a diffraction limited area [70].

$$d \approx \frac{\sigma_x}{\sqrt{N}} \tag{1.1}$$

The stochastic switching behavior is a consequence of: oxidation and reduction reactions happening between the fluorophore and the imaging medium, stimulated by illumination with laser powers high enough to trigger the transition of the molecule from singlet state to triplet state. Triplet state is an intermediate state where the electron is still in a high energy level, without recovering to ground state and therefore not emitting a photon. After being able to have one emitter at a time in a diffraction limited area, the individual emitter positions can be extracted by fitting the emitter signal, by an appropriate PSF model function (**Figure 1.4 c**) which is an estimate between molecular position and its intensity, before they bleach (enter in a permanent dark state). A two dimensional Gaussian for example, described in the next equation [67],

$$h_G(x, y\,|\theta) = \frac{\theta_N}{2\pi\sigma^2} \times e^{\left(-\frac{(x-\theta_x)^2-(y-\theta_y)^2}{2\sigma^2}\right)} + \theta_0 \tag{1.2}$$

$h_G(x, y\,|\theta)$ represent the photon count at position (x, y), knowing the parameters $\theta = \{\theta_x, \theta_y, \theta_N, \theta_0\}$ .Here, θ_x, θ_y are coordinates of the emitter center, $\theta_N$is the total number of photons, θ_0 is the background offset (signal coming from the background that is neither from camera baseline nor from the molecule itself) and σ is the width of the fitted Gaussian in the respective direction (x or y in 2D) [63].

The fitted signal comes from raw images, as represented in **Figure 1.4 b**. Hence, it is critical that the acquisition is performed by cameras with high quantum efficiency and pixel size matching Nyquist criteria. Normally, EMCCD (Electron Multiplying Charge-Coupled Device) or sCMOS (Scientific Complementary Metal Oxide Semiconductor) devices are used for this ending. EMCCD have a higher quantum efficiency, lower read noise but suffer from excess noise per pixel (consequence of the probabilistic nature of the electron multiplying gain). sCMOS have a smaller quantum efficiency and higher read noise but they don't suffer from excessive noise per pixel and can enable much faster acquisitions. Besides, when the number of collected photons is high enough, sCMOS can perform better than EMCCD cameras [71,72].

2 Materials and Methods

2.1 Cell Culture

Neuroblastoma Neuro2a (N2a) cells (ATCC CCL-131) are a mouse neuroblastoma cell line. These cells are like neuronal precursors that can differentiate into neurons, and are able of unlimited proliferation *in vitro*. N2a cells were grown in Dulbecco's Modified Eagle Medium (DMEM) (DMEM + GlutaMAX supplement, Gibco, Life Technologies) supplemented with 10 % fetal bovine serum (FBS) (Sigma-Aldrich) in a humidified incubator at 37 °C with 5 % CO_2. After reaching 80-90% confluence they were washed once with phosphate buffered saline (PBS, pH 7.4) (Gibco, Life Technologies) and trypsin (Life Technologies) was added to dissociate adherent cells from the dish. After trypsin addition, cells were incubated 5 minutes at 37 °C with 5 % CO_2. Trypsin activity was stopped by adding complete medium (DMEM + GlutaMAX supplement + 10% FBS). To maintain cell culture, the resulting cell suspension was split in a dilution of 1:10 to a dish. Cells were counted using a Neubauer Chamber and platted in different amounts to perform different experiments. 150 000 cells per mL were plated to evaluate the effect of CD2AP *wild type* and *mutant form* on early endosomes. To assess the effect of CD2AP downregulation (siRNA for CD2AP) on F-actin patterns and their relation with early endosomes, 50 000 cells per mL were plated to reach the best confluence after 72h of incubation.

2.2 DNA Transfection

N2a cells were plated in glass coverslips inside a 6-well plate and cultured in complete medium in 5% CO2 at 37 °C. After 24h of culture, the confluence was about 80%–90% and cells were transiently transfected with 0.5µg of cDNA with Lipofectamine 2000 (Life Technologies). Cells were analyzed after 24h of treatment. We used the following DNA plasmids encoding: CD2-associated protein in expression vector pEGFP, hereafter referred as *wild type,* and gently ceded by M. Cormont (University of Nice); CD2-associated protein with a gene variation on the 633 position (K633R) in expression vector pEGFP, hereafter referred as the *mutant form*; the empty vector pCS2 with GFP; and also, Rab5 in expression vector pEGFP, a gift from M. Arpin (Institut Curie).

2.3 siRNA Transfection

For small interfering RNA (siRNA) treatment, N2a cells were transiently transfected with 10 nM specific siRNA with Lipofectamine RNAiMax (Life Technologies). The amounts and volumes are given on a per well basis. The following siRNA oligonucleotides were used: as siControl a non-targeting control siRNA (10uM) (UUC UCC GAA CGU GUC ACG UTT ACG UGA CAC GUU CGG AGA ATT) (Life Technologies) and for knockdown of CD2AP, siCD2AP (10uM) (Santa Cruz). Cells were analyzed after 72 h of treatment. When indicated, cDNA was transfected after 48 h of siRNA treatment and cells were analyzed after 24 h (when transfecting with Rab5).

2.4 Immunofluorescence

Cells were washed 2 times with PBS 1X to remove the reminiscent culture medium. They were then fixed with PFA/PEM solution (**Appendix A**) in order to preserve the actin cytoskeleton the best way possible

[73] for 10 min, after which were washed four times with PBS 1X. After this, cells were permeabilized using a solution of 0.1 % (w/v) of saponin (Sigma Aldrich) in PBS 1X for 30 minutes. Then, cells were washed with PBS 1X four times and blocked using a solution of 2 % (w/v) BSA (Sigma-Aldrich) in PBS 1X for 30 minutes, washed again with PBS 1X four times. After this cells were incubated at 4 ºC overnight with primary antibodies (**Appendix A**). Cells were then washed four times with PBS 1X to remove the excess of primary antibody. Appropriate secondary antibodies or probe (**Appendix A**) diluted in blocking solution were used for 1 hour at room temperature. After washing four times with PBS 1X, cells were fixed again in PFA/PEM solution for 5 minutes and washed four times with PBS 1X.

2.5 Imaging Medium Preparation

Before dSTORM acquisitions, samples were mounted in concave slides (VWR) using a modified version of the imaging buffer previously reported in several studies [70,74]. All the intermediate solutions are described in the **Appendix A**. It is composed by 140 µL PBS 1X (74.6 %), 20 µL MEA (10.6 %), 20 µL Glucose 40 % (10.6 %), 4 µL cyclooctatetraene (2.1 %) and 4 µL oxygen scavenger (2.1 %). Slides were then sealed with twinsil (Picodent). Percentages indicate solution volume fraction.

2.6 Image Acquisition and Analysis

Images were acquired on a custom made system based on a Nikon Ti microscope body, equipped with a sCMOS camera, Hamamatsu Flash ORCA 4.0, using the a Nikon 100X 1.45 NA Oil immersion objetive. A 642 nm Vortran Stradus was used to excite Alexa-647 at 350 W/cm^2. For maximum specificity a Chroma 640LP filter for 642 excitation were used. Images were acquired with MicroManager microscope control software [75]. Each acquisition was composed by 20000 frames with an exposure time of 10 ms. Reconstructed images using ThunderSTORM [76] were rendered to a pixel size 10 times smaller than the camera pixel size, yielding to a pixel size in dSTORM images of 14.1 nm x 14.1 nm. The output of ThunderSTORM is in the form of pointillist x-y coordinates of the localized fluorophores that can have up to millions of entries. All measurements are performed in RStudio [77], a free and open-source integrated development environment (IDE) for R, a programming language for statistical computing and graphics. Before feeding the coordinates of the localized emitters to Rstudio every list passes through an optimization protocol that includes choice of ROI (**Appendix B**), population culling and a merging algorithm (explained and discussed **section 3.2.2**). F-actin pattern study and measurements are described in **Appendix D**. All the data is presented as mean ± SEM (Standard Error of the Mean).

3 Results and Discussion

3.1 dSTORM vs Conventional Fluorescence Microscopy

In this section we discuss the improvement in resolution offered by dSTORM when compared with conventional epifluorescence imaging but also the main challenges arising when using dSTORM. For that we used F-actin super resolved images acquired in our setup (described in **section 2.6**).

Colocalization of signal is a strong indicative of protein interaction in biology. However, the resolution in conventional epifluorescence imaging is limited and so is the certainty of this colocalization. Super resolution like dSTORM enables to see under the PSF and detect colocalization with more accuracy.

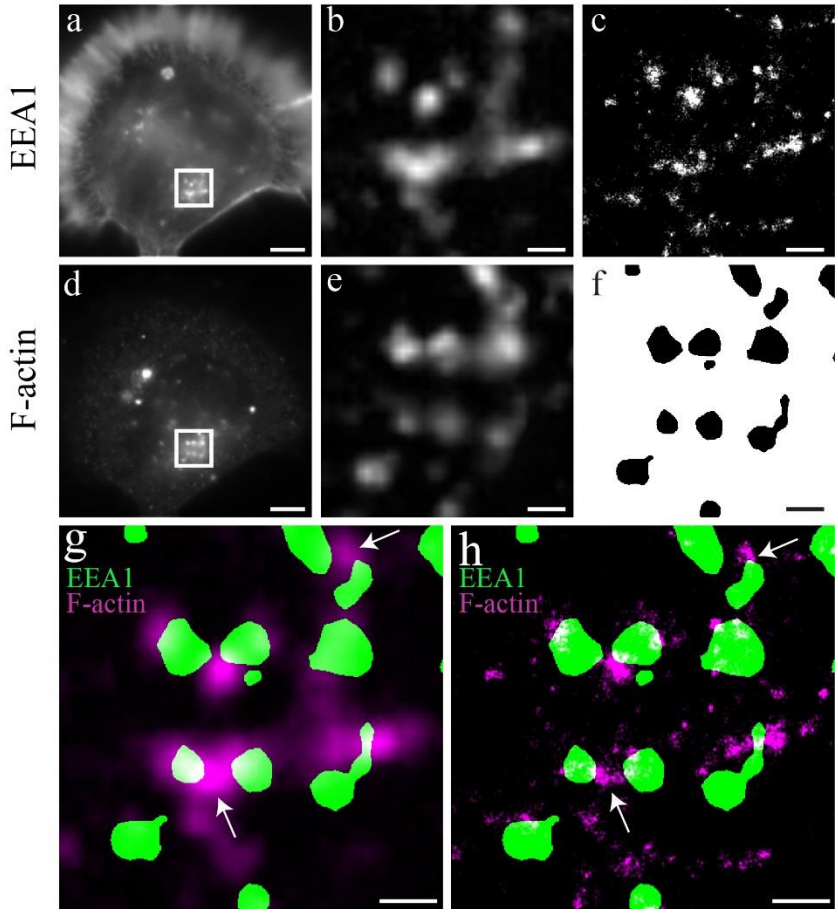

Figure 3.1 - Comparison between conventional epifluorescence microscopy and dSTORM. **a), d)** Epifluorescence images of N2a cells stained with phalloidin and EEA1 antibody, respectively. **b), c)** White boxes magnification a) and d) respectively. Background was subtracted to visualization purposes. **c)** dSTORM reconstruction of b). **f)** Endosome segmentation of e). **g)** Merging of b) and f). Some Endosomes colocalize with F-actin epifluorescence signal. **h)** Merging of c) and f). White Arrows indicate areas with clear differences of colocalization with conventional epifluorescence microscopy vs colocalization with super resolution. Scale bars: **a, d** 5 µm. **b, c, e, f, g, h** 1 µm

As observed in **Figure 3.1** the epifluorescence signal is broader than the signal in dSTORM images. The points of highest intensity match both in epifluorescence and dSTORM, indicating that a higher intensity in an epifluorescence image corresponds to a higher presence of the labelled protein. The blob like signal

is much smaller in dSTORM images because it is no longer limited in resolution. This difference leads to an apparent colocalization of signal in epifluorescence images that in the end is just a superimposition of the molecule PSF's, as exemplified in **section 1**, **Figure 1.4 d**. This can lead to erroneous conclusions of protein-protein interaction. For example, in **Figure 3.1 g** the top white arrow indicates an area where the F-actin seems to colocalize with both endosomes. In **Figure 3.1 h** we see that in the same area there is only colocalization between the F-actin agglomerate and one of the endosomes. Besides improving colocalization analysis, dSTORM also enables the visualization of structures unresolvable by epifluorescence microscopy. In this case it is very important to note that although this is a technique that enables resolutions of a few tens of nanometers, it also requires a great deal of optimization, especially in terms of labeling (further discussed in **section 3.2.3**), and could introduce different kinds of artifacts. One also will never have 100 % certain of every detail presented in a super resolution image because there are many sources of possible errors [78]. **Figures 3.2 b) and e)** represent epifluorescence and dSTORM reconstruction of the same area, respectively. One can clearly see that there is a huge improvement in the detail between both images. The resolution improvement is due to the sub pixel localization and because of it, one can transform each pixel in image **b)** in 10 pixels in image **e)** (reconstruction input of our implementation), and map detections with sub pixel accuracy. This procedure is explained in detail in **section 3.2.1**.

To answer the question "Is the structure, approximately, real?" there are two common methods. The first one is to screen a lot of samples, increasing the comparison population of the structures in study, to establish common characteristics or to average the resultant images to have a better approximation of the real structure [79]. The other one is to image known and well characterized structures like microtubules, the Nuclear Pore Complex (NPC), the space between the pre and postsynaptic cell, among others. They have an expected output and could also serve has a calibration method or a setup optimization tool to other error sources like setup temperature, exciting wavelength and intensity, coverslip thickness, refractive index mismatch between the lens immersion media and the specimen and imaging medium composition [80]. Having said this, **Figure 3.2 e)** is only a possible structure of its corresponding epifluorescence image. Resolution wise, **Figures 3.2 c) and f)** also translate the improvement given by this technique.

The resolution measurement given by the Full Width at Half Maxima (FWHM) in **Figure 3.2 g)**, a common method to measure resolution, is only an approximation because the place of choice for the measurement has associated errors like labeling density variability, local SNR or changes in the structure itself [81]. Again, multiple measurements are necessary in order to achieve an average with high enough confidence and associated errors [78].

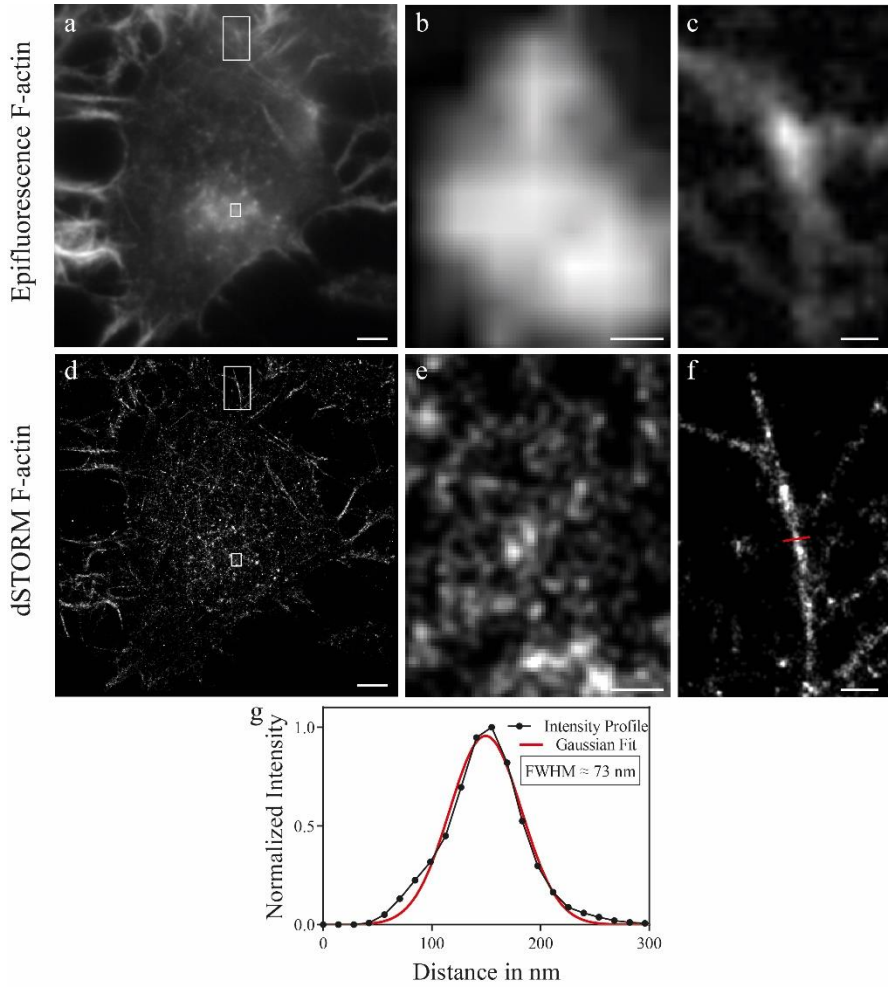

Figure 3.2 - dSTORM enables sub diffraction limit imaging and higher resolution. **a)** Representative N2a cell labeled for F-Actin. **d)** dSTORM image of a). **b)** and **c)** Epifluorescence magnifications of white boxes in a). Both images were background subtracted for enhanced contrast. **e)** and **f)** Magnifications of white boxes in d). No longer being diffraction limited, the images enable to b) with higher detail. **g)** Transversal measurement of the branch represented in f) (red line) shows a branch width of 73 nm. Super resolution measurements are performed by fitting the intensity profile along a line and fitting it to a Gaussian curve. The Full Width at Half Maxima (FWHM) indicates an approximate value for the distance measurement and it is defined as $FWHM = 2.35 \times \sigma_x$, where σ_x is the standard deviation of the Gaussian fit of the intensity profile. Scale bars **a, d** 5 µm. **b, e** 200 nm. **c, f** 500 nm.

Compared with conventional epifluorescence, dSTORM offers an important improvement in resolution but also increased error sources that must be dealt with optimization and with a considerable sample size to reduce possible artifacts coming from those error sources.

3.2 dSTORM, Single Molecule Detection and Quantitative SMLM

Another important feature discussed in this section about dSTORM is the possibility of having access to individual locations of the detected molecules and being able to quantify them. This enables new kind of analysis but also to the necessity of implementing certain protocols to prevent errors caused by fluorophore behavior or by poor detections [82–87].

3.2.1 Detection Protocol

Figure 3.3 a shows an epifluorescence image where all fluorophores are emitting at the same time. After illuminating the sample with a laser matching the absorption spectrum of the fluorophore and with enough power, the sample starts to show a switching behavior, illustrated **in Figure 3.3 b**. The fluorophore changes between bright and dark are transient and stochastic and each frame shows a stochastic subset of molecules in the ON state (activated). After having acquired enough frames similar to **Figure 3.3 b**, ThunderSTORM sweeps to every frame and starts by identifying single emitters by filtering the raw acquisition frames (**Figure 3.3 c**) and applying a threshold to the pixel intensity values obtained in the filter output image. Our filter settings were chosen according to *Ovesny, 2016* [63] and our threshold was set to 2.2 times the frame pixel intensity values standard deviation. With lower threshold values, it was visually inspected that a lot of detections were coming from background fluctuations and not only from those bright spots observed in **Figure 3.3 b**. These background fluctuations are unwanted and could arise from emitters out of the Field of View (FOV). After this step, the filter output images are analyzed and the pixels with the highest intensity in an 8-connected neighborhood (a 3 × 3 matrix around central pixel) are set to be a putative emitting fluorophore. If these pixels have a higher value than the defined threshold they are considered an emitting fluorophore and the approximated location of the molecule is set to that pixel (**Figure 3.3 d** red dots and **Figure 3.3 e** red square).

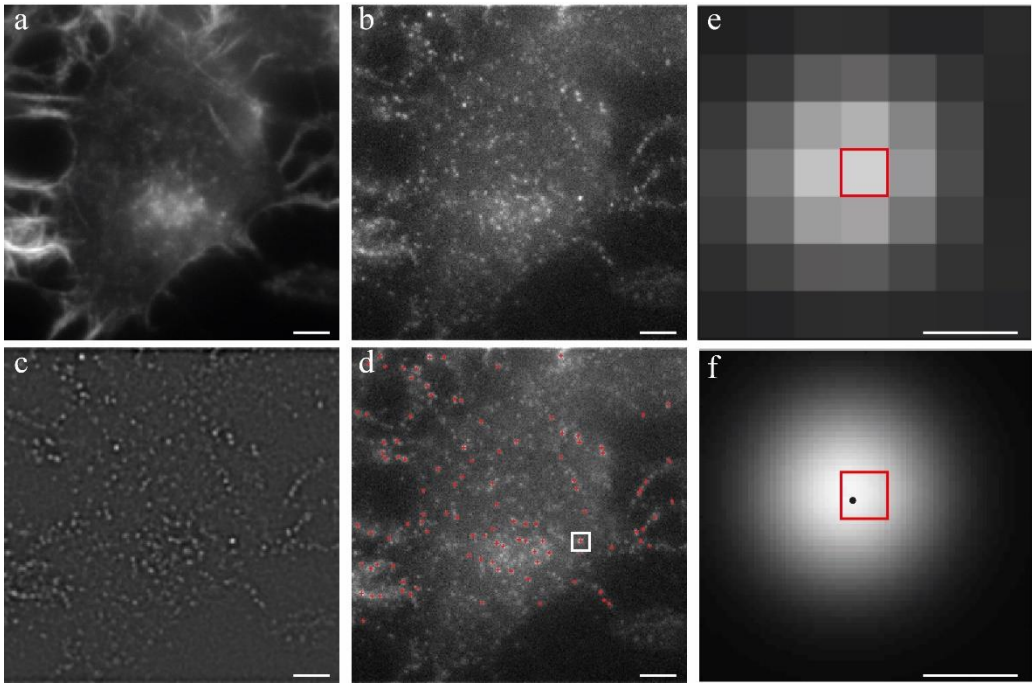

Figure 3.3 - Detection protocol in dSTORM experiments. **a)** Epifluorescence image of N2a cell with labeled F.actin. **b)** Representative frame of dSTORM acquisition. The small light dots represent labeled F-actin molecules stochastically activated. **c)** Filtered frame of b). **d)** After identifying local maxima in c) that fulfill threshold requirements a set of approximated locations of molecules is determined (red dots in d). **e)** Sub image around identified emitter in d (white box) Red square is the pixel with highest intensity and the approximated location of the emitter. **f)** PSF Gaussian fit of e) and sub pixel emitter localization by least square fitting (black dot). Scale bars **a-d** 5 µm. Scale bars **e, f** 280 nm.

In every dSTORM experiment there is a time interval where the fluorophores are being induced to the metastable dark state, characterized for a high density of emitting fluorophores. Therefore we only included in our analysis the molecules detected after 10000 frames, allowing for the fluorophores to enter the metastable dark state and giving a margin to reach an equilibrium state where they switch between the *on* and *off* states as much separated from each other as possible. This leads to a compromise between erroneous detections undetected emitters because they could bleach completely before detection, also considered as an artifact [78]. A sparse activation of the emitters is vital when using an algorithm for sub pixel localization that assumes to be only a single activated emitter present in the sub-image where the localization is performed [63,78,80]. With our settings, a sub-image corresponds to an area of 7 × 7 pixels centered on the pixels of the molecules approximated locations (**Figure 3.3 e**). If we take our system pixel value (141 nm x 141 nm) this results in a square of 987 nm × 987 nm. The choice of this area is based on the PSF geometry of the fluorophore in question. That could be determined or approximated with a high confidence if we run the algorithm in a few frames, in the same conditions of our experiments [88]. We observed that the standard deviation of the fitted Gaussian (σ) profiles had a mean value around 180 nm (that is equivalent to 1.3 in pixel units). According to ThunderSTORM creators guidelines the fitting radius should be an integer close to the value 3 × σ [88]. The reason is because the fitting is going to assume a Gaussian profile of the PSF. Values of 3 × σ in this profile means that there is a 99.73 % of probability of the real emitter center to be within this area. By choosing a fitting radius of 3 pixels we are using a value of 2.3 × σ which means that we are between the known percentiles of 2 × σ (95.44 %) and 3 × σ (99.73 %). The other alternatives were a fitting radius of 2 pixels or 4 pixels that would lead to an area of 564 nm × 564 nm and 1128 nm × 1128 nm, respectively. Even though 4 pixels would lead to an area broad enough to ensure a probability > 99.73 %, the sub image area would be 1.3 times bigger than the one with 3 pixels, increasing the probability of finding another molecule in the same area. On the other hand, with a fitting radius of 2 pixels we would be only between 1 × σ (68.26 %) and 2 × σ (95.44 %), losing too much localization precision. Solutions based on *Multi Emitter Fitting* algorithms [89] enable more than one emitter per sub image but the image processing is very time consuming so we choose speed at the cost of some inaccurate detections. After having the sub image the raw image is approximated by a PSF function following a Gaussian model (**Figure 3.3 f**) (**equation 1.2**), where the difference between the intensity observed in the raw image (**Figure 3.3 e**) and the value returned by **equation 1.2** is minimized by the least squares fitting method. The position where that happens is the subpixel location (**Figure 3.3 f, black dot**).

3.2.2 Population optimization

After having sub pixel localizations of emitters, we still needed to optimize our population. First of all, fluorophore behavior is very dependent of the nano environment that influences its photophysical properties [63,78,80]. It was also already reported that standard deviations of the fitted Gaussians (σ) are normally distributed around expected values (fluorophore characteristic) [86] and in our experiments they were indeed approximately described by this distribution. To further guarantee that the sub-pixel localization was correctly done, we excluded detected emitters based on (σ) and intensity values. To know the acceptable interval we needed a population on which we could make decisions based on the distributions (σ). So, we first restricted the analysis to the ROI, removed the localization performed in the first 10000 frames, limited

the intensity per detection to 10000 photons and also removed emitters with a standard Gaussian deviation bigger than 400 nm (false detections). Having our population we limited the acceptable σ interval to $\mu \pm 1.5 \times S$ [86], represented in **Figure 3.4**,

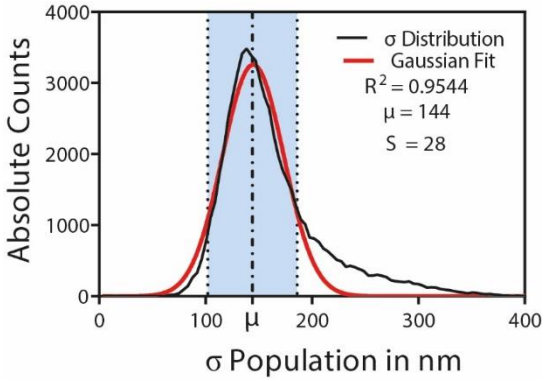

Figure 3.4 - Population culling based on the standard deviations (σ) of the fitted PSF model. The resultant distribution after restricting to the ROI, removing the first 10000 frames as well as emitters exhibiting a photon count superior to 10000 and a sigma superior to 400 nm is given by the black curve. A Gaussian fit is performed and the interval of σ is calculated based on the standard deviation of this fit (S). The interval (light blue) is defined as $\mu \pm 1.5 \times S$, where μ is the mean of the fitted Gaussian.

This procedure removes detections originating from multiple emitters in the same sub image that are the most likable reason for the distribution to stretch towards the right because multiple emitters increase the size of the PSF. The smaller values being filtered could represent detections originating from background fluctuations.

The last step was to apply a merging algorithm [86,87,90,91] that is of the most importance since we are studying the F-actin patterns distribution, counts and clustering. Not applying it has been reported as one of the most frequent artifacts in quantitative SMLM [78,80,84]. In **Figure 3.3 b** is represented a single frame exhibiting some of the fluorophores in the ON state. The rate at which these fluorophores go back to ground state is also stochastic, which means that some could be ON through 5 frames while others could be through 10 or 15 frames. ThunderSTORM performs emitter detection frame by frame and the detection protocol that we already discussed in **section 3.2.1** is repeated every frame. This means that if an emitter stays in the ON state longer than one frame it will be erroneously considered as a different molecule in the next frame and localized at approximately the same position (approximately because there could be slight variations in the emission profile that lead to slightly different sub pixel localization). So, in order to correct this undesirable situation when doing cluster analysis and studying patterns we had to know until what distance emitters appearing in consecutive frames are still considered the same one and merging all consecutive detections of that same emitter into a single detection. The distance threshold criteria we used to merge was a function of localization uncertainty without any temporal capping (for how long this consecutive blinking lasts), **Figure 3.5**. Similarly, to the σ parameter, we could also have a distribution of localization uncertainty with a Gaussian shaped error. In practice, an emitter is localized but its exact position has always an error associated with the system acquisition instrumentation, nano environment conditions, and

fluctuations in the emitter photon emission among others. In our implementation, the approximate value for uncertainty is mathematically given by,

$$(\Delta\hat{\theta}_{xy})^2|_{LSQ} = \frac{g\hat{\theta}_{\sigma^2} + \frac{a^2}{12}}{\hat{\theta}_N}\left(\frac{16}{9} + 4\tau\right) \quad (3.1)$$

$$\tau = \frac{2\pi(\hat{b}^2 + r)(\hat{\theta}_\sigma^2 + \frac{a^2}{12})}{a^2\hat{\theta}_N} \quad (3.2)$$

Where $(\Delta\hat{\theta}_{xy})^2|_{LSQ}$ is the uncertainty of the emitter localization by least-squares method (our choice), $\hat{\theta}_{\sigma^2}$ is the standard deviation of the fitted Gaussian PSF in nm, a is the pixel size in nm, $\hat{\theta}_N$ the estimate of the number of photons to a given emitter, b the background signal (standard deviation of the residuals between raw data and the fitted PSF model and g and r correction factors dependent of the type of camera used (in our case sCMOS being both equal to 2) [63]. Since the average localization precision of single emitters in our dSTORM experiments can be determined by fitting a normal distribution to our population uncertainty values, the 2-dimensional Gaussian PSF error profile would have a maximum of 3 times the acquisition average uncertainty value. An emitter has 99.7% probability of being within an area with radius equivalent to 3 times of the PSF [90]. Having performed this merging step we reduced putative clusters originating from a single fluorophore emitting through several consecutive frames and an over counting of emitters since many localization were merged into a single localization. This procedure is very important when performing quantitative kind of analysis in dSTORM experiments [87]

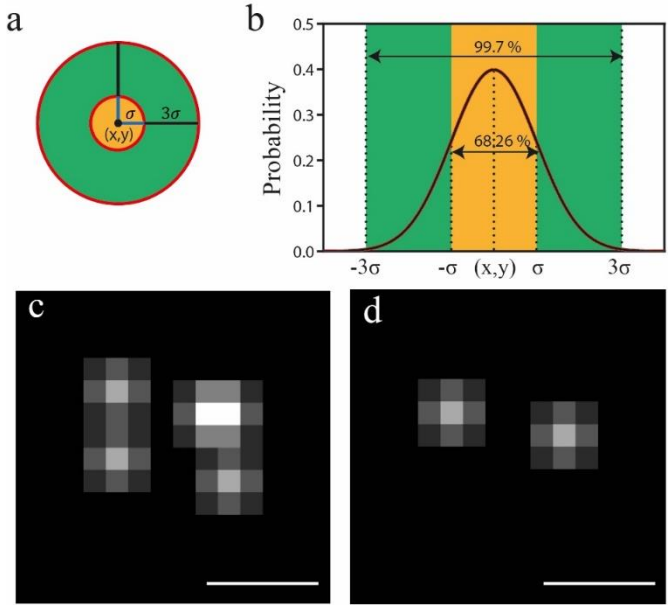

Figure 3.5 - Localization uncertainty and merging same molecules appearing on consecutive frames. **a)** Top view representation of the sub-pixel localization of a molecule. Its center (x, y) is determined with an associated uncertainty. Using a Gaussian error model the uncertainty values correspond to the standard deviation of the Gaussian curve for molecular position (σ) and we can determine the known quantile 3σ. **b)** Transversal view of a).The percentages indicates the probability of having the molecule in a circle with radius corresponding to σ (yellow) and 3σ (green). **c)** Detected molecules in 15 consecutive frames without applying the merging algorithm. **d)** c) after applying merging algorithm. Scale bars 70 nm.

3.2.3 dSTORM Phalloidin Labeling

Another important aspect when using dSTORM is the labeling itself. This is a technique that uses a lot of computational processing power to complete all the calculations necessary to obtain the super resolution image. But even with the perfect processing steps, meaning without input errors and an ideal acquisition system, the final image could not be corresponding with the real structure. This is due to the fact that the labeling of a structure "increases" the size of the structure that is now composed by the protein plus the probe with the fluorophore. Besides that, when dealing with known and unknown structures, it is important to perform labeling density studies to ensure the desired local density because of the random nature of probe binding. Furthermore, it was demonstrated by Nyquist and Shannon and *Legant et al, 2016* [81] that the desired resolution is only obtained if there is a labeling density high enough to ensure the presence of two fluorophores separated by a distance that must be half of the desired resolution. For example, if the primary/secondary antibody increases the effective size of the protein by 20 nm, the resolution is already limited to 40 nm. Although we didn't study the labeling density in this work, we still optimized the process by staining the actin filaments with phalloidin probes instead of primary and secondary antibody typical staining. When comparing with primary/secondary antibody complex with phaloidin staining the possible obtainable resolution goes from 40 nm to 5 nm. Phalloidin is a toxin that binds with high affinity to F-actin and has the size in the order of the 10 Å to 20 Å, and thus compatible with dSTORM [92,93] .

3.3 F-Actin Correlation with Early/Late Endosomes

To study the F-actin patterns in N2a cells and to determine if the perinuclear F-actin is more associated with early or late endosomes we resort to the mapping capabilities of dSTORM. After culturing and fixing N2a cells, the protein of interest, F-actin, was stained with the conjugate Alexa647-phalloidin. Since EEA1 and LAMP1 are proteins characteristic of the early and late endosomes, respectively we co-stained cells with primary antibody against EEA1 or with primary antibody against LAMP1. We repeated this experiment twice but there were some technical difficulties with the image acquisition in one experiment and thus the results are not included in the thesis. In the excluded experiment was obtained a very different number of F-actin particles detected between cells stained against EEA1 and cells stained against LAMP1. In fact, if we consider the mean number of F-actin particles detected per cell there is a variation of almost 100 % between the two staining conditions. This can be explained by a deficient staining or by an insufficient imaging medium penetration into the cells.

Differential and uneven staining is avoided as much as possible by staining both conditions at the same time, with the same preparations of phalloidin. On the other hand, the preparation of the imaging medium is done individually for each sample. If the buffer fails to reach the cells effectively, all the dynamic changes between triplet and singlet state are altered. Moreover, the blinking behavior is known to be linked to an environment without oxygen, being the oxygen scavenger present in the buffer critical to this end [70]. If the blinking behavior is not efficient it will influence the detection of fluorophores. Having into account this big variation of F-actin particles, and since we are studying spatial patterns and their distributions, we decided not to include those results. In the second experiment, the mean variation of F-actin detections between conditions was 14 %. It is hard to say if this is acceptable or not, however it is perfectly normal to

have a variation in the number of particles as there are a lot variation sources, for example: metabolic or cell cycle status of the cell, or heterogeneous labeling density. All the measurements should be interpreted as relative variations, tendencies or averages instead of absolute counts.

Before looking into the F-actin patterns we measured the presence of both types of endosomes in the perinuclear area because this is also an indicative of the putative relation between actin and both types of endosomes (**Figures 3.6 a-f**).

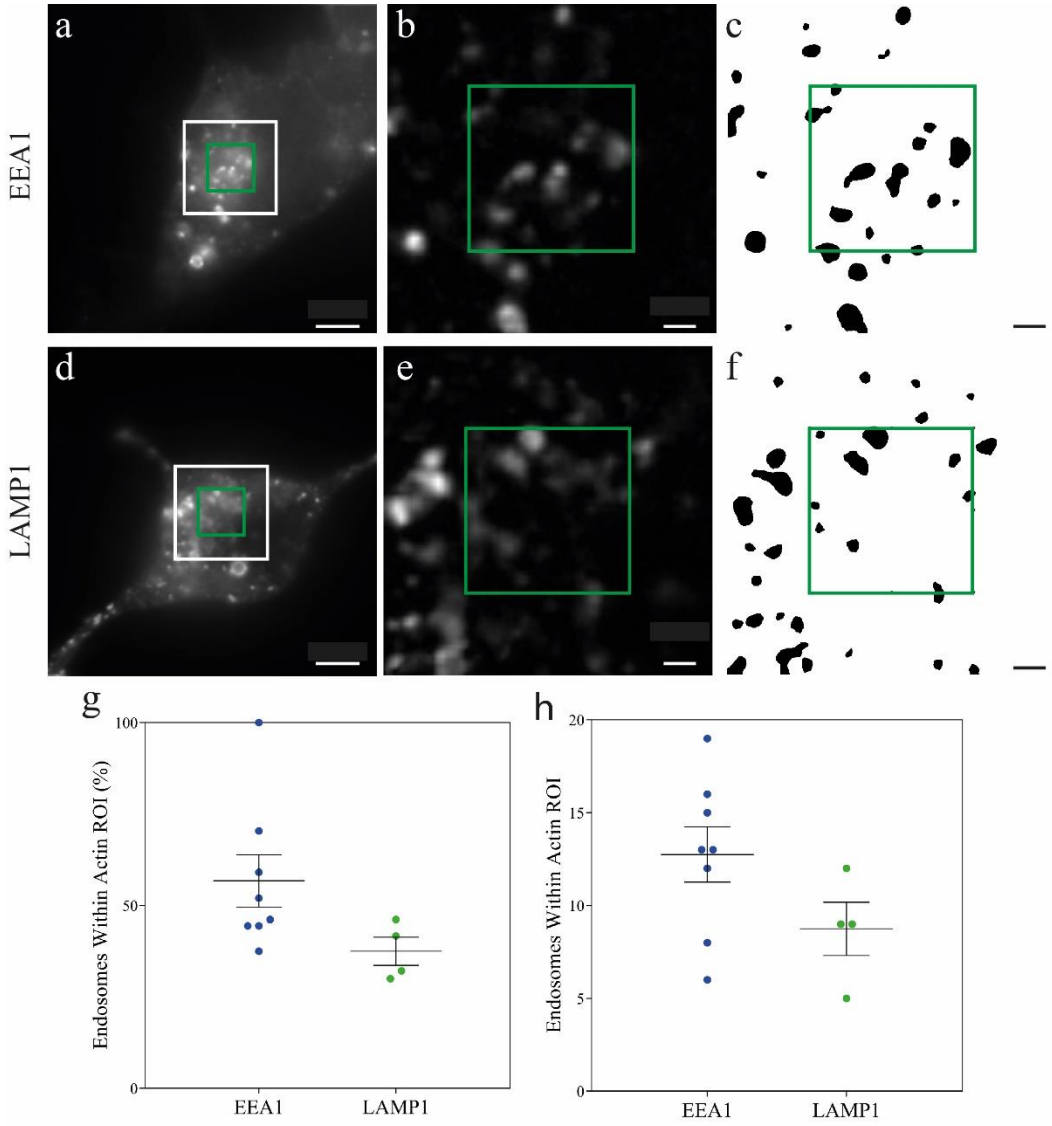

Figure 3.6 - Early endosomes are more present in the perinuclear region than late endosomes. **a), d)** Representative epifluorescence images of N2a cells with labeled early endosomes and late endosomes. The white frame indicates endosomal ROI and green frame indicates Actin ROI. **b), e)** White frame magnification of a) and d) respectively and background subtraction for visualization purposes. **c), f)** Endosome segmentation (See Appendix B). **g), h)** Early and late endosome quantification within Actin ROI (green square) in percentage and absolute counts, respectively. Scale bars **a, d** 5 µm. Scale bars in **b, c, e, f** 1 µm.

We observed that there are more early endosomes in the region rich in actin puncta, the perinuclear region (**Figures 3.6 g and h**). In previous results from our lab, these actin puncta were found to colocalize often with early endosomes as observed by confocal fluorescence microscopy. This indicates that the F-actin puncta are clusters of actin filaments polymerized at the early endosomal membrane [18]. These structures have been described associated with endosomes of non-neuronal cell to control tubule fission and endosomal maturation [38,39].

To better characterize this endosomal F-actin in neuronal cells we compared the distance of each F-actin detection to endosomes present in the perinuclear region. For that we calculated the distance between the position of each dSTORM detection and the nearest endosome, considering the perimeter of the segmented endosome, to obtain the percentage of F-actin detections in the vicinity of endosomes (**Figure 3.7**). It is important to note that each F-actin particle is only linked to the nearest endosome, ensuring no repetitions when obtaining the results. This analysis demonstrated a higher percentage F-actin detections in close range to early endosomes than to late endosomes. Interestingly, we observed a steep increase in the percentage of F-actin detections in close range with early endosomes. On average about 20 % of the F-actin is detected at a 20 nm distance of an early endosome. On the contrary, only 6 % of the F-actin is detected at a 20 nm distance of late endosomes, indicating a preference towards early endosomes. These can be consequence, as shown in Figure 3.5 h, of the superior number of early endosomes present in this region.

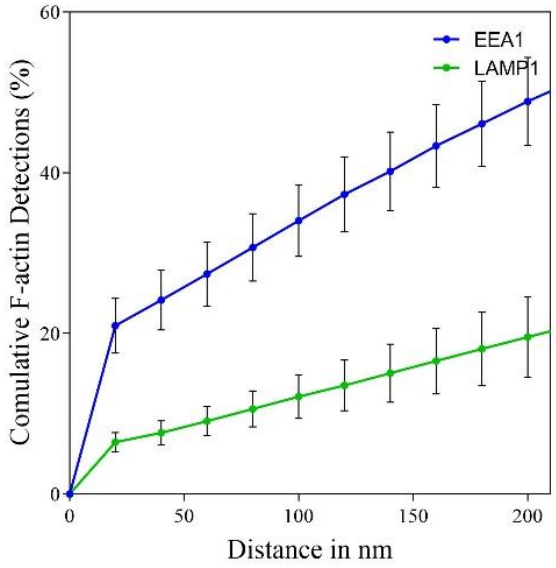

Figure 3.7 - Distance between F-actin detections and endosomes. The lines are the result of the averaging between F-actin patterns in all cells analyzed for each type of endosomes. Distribution plot until 210 nm with a measurement every 20 nm. Every 20 nm is measured the percentage of F-actin. The slope in the curves is proportional to the increase in F-actin detections in each 20 nm interval.

After having a general distribution of F-actin detections relative to endosomes, we also inspected the F-actin fractions and quantities present within a certain threshold distance from each endosome. We choose 50 nm as threshold distance because it is 2.5 times the 20 nm distance at which we observed the

greatest increase of F-actin detections. We measured the percentage of the total detections to eliminate sample variability, **Figure 3.8 a)**, but also of the absolute counts, **Figure 3.8 b)**, to eliminate the potential bias introduced by the choice of a ROI.

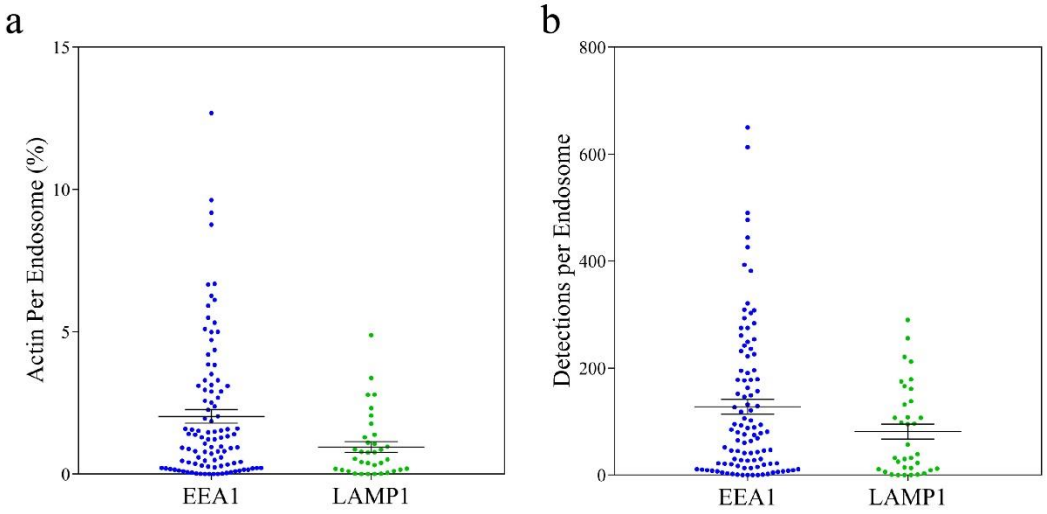

Figure 3.8 - Quantification of F-actin detections per endosome. A threshold of 50 nm was fixed for each endosome. **a)** F-actin detections per endosome as percentage of the total F-actin present in the interest ROI. **b)** Absolute F-actin detections per endosome in the same ROI.

Together the dSTORM analysis suggest that an early endosome has, on average, more F-actin in its surroundings than late endosomes, supporting the initial epifluorescence data. F-Actin found associated with late endosomes may originate from either novel polymerization at late-endosomes or from remaining partially associated during early endosome maturation [18,38,39].

In biology a lot of interactions occur through clustering events [91]. Besides that, it is known that mechanisms present in sorting events usually require a pressure source either to separate tubules from their endosome parents or possibly in invagination processes, since they require membrane deformation. So, it is logical to think that, having a greater concentration of protein, there is also a greater exertion of pressure. The main challenge in this analysis is to differentiate between clusters and non-clusters. Normally, if the protein in study is already well documented and there are certain parameters that tend to occur, like number of particles per cluster or cluster size, and one can always follow these metrics and have an output supported by the literature. In our case we are studying F-actin patterns that, to our knowledge, are not characterized in this way. So, in order to be able to identify these clusters we had to find a way of standardize the inputs that will define what belongs to a cluster and what does not. We decided to implement an empirical strategy based on DBSCAN [94], a density based cluster algorithm, described in the **Appendix C.**

Having identified F-actin clusters, we performed a cluster colocalization analysis by determining the fraction of endosomes within 20 nm of a cluster.

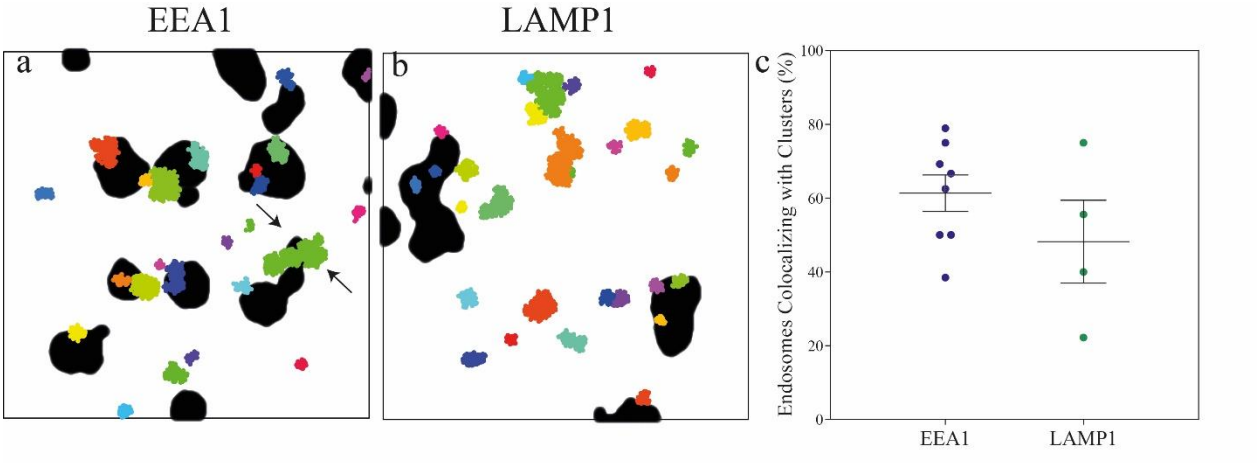

Figure 3.9 – F-actin clusters exhibit more colocalization with early endosomes than with late endosomes. **a), b)** show a representation of F-actin clusters (colored aggregates) and early and late endosomes (black islands), respectively. The black arrows shows what seems to be endosomal tubule with a big cluster. **c)** Shows the percentage of endosomes in the Actin ROI colocalizing with a F-actin cluster.

Early endosomes are, on average, more associated with F-actin clusters than late endosomes (**Figures 3.9 a-c**), further suggesting that the F-actin present at late endosomes might be originated at early endosomes and some of its remains might still persist after maturation processes. However, this is a preliminary result that needs to be confirmed with more experiments. Interestingly we could observe in one endosome (arrows) an actin cluster (green) associated with an endosomal tubular extension (**Figure 3.9 a**).

From all our results, we can conclude that early endosomes are more present in the perinuclear region where F-actin puncta is enriched and that F-actin is associated with both early and late endosomes. Importantly, there seems to be overall more F-actin and bigger association of F-actin clusters at early endosomes.

3.4 F-Actin Patterns and CD2AP

In this section, we studied the impact of silencing CD2AP on perinuclear F-actin. CD2AP was knocked down using specific interference RNA following a standard protocol implemented in our lab that results in around 90 % decrease of CD2AP levels. The F-actin staining protocol was the same mentioned in the previous section but early endosomes were labeled with a plasmid encoding Rab5 and we did not label late endosomes.

We started by analyzing the number of F-actin detections in CD2AP knockdown (KD) cells (siCD2AP) compared to cells treated with non-targeting siRNA (siCtrls). When observing a control cell, by epifluorescence, it had bright puncta in the perinuclear region, consistent with high clustering of F-actin in those locations (**Figures 3.10 a, b**). On the contrary, the intensity of these puncta was greatly decreased in CD2AP KD cells show a great decrease in (**Figures 3.10 d, e**). Since intensity is correlated with the amount of probe binding to F-actin, we predicted a decrease in dSTORM detections of F-actin in cells KD for CD2AP. Indeed, we obtained a reduced number of F-Actin detections and they seem more scattered in CD2AP KD cells (**Figure 3.10 f**) as opposed to control cells (**Figure 3.10 c**). To confirm this we plotted the number of

detections per cell and computed the nearest neighbor distance to analyze the compactness of F-actin detections (**Figures 3.10 g and h**). We found a considerable reduction of 64 % in mean F-actin detections in CD2AP KD cells and the resulting patterns were less compact. It is important also to refer that applying the merging algorithm explained in **section 3.2.2** enabled a more accurate nearest neighbor measurement by avoiding distances of almost zero because of multiple consecutive detections, likely resulting of the same molecule. In the literature, CD2AP was found to interact with proteins involved in F-actin polymerization like cortactin [13,17]. Cortactin interacts directly with the Arp2/3 complex, crucial for actin polymerization and therefore to the increase of actin particles [95,96]. The lack of recruitment of cortactin may explain the overall reduction in F-actin observed.

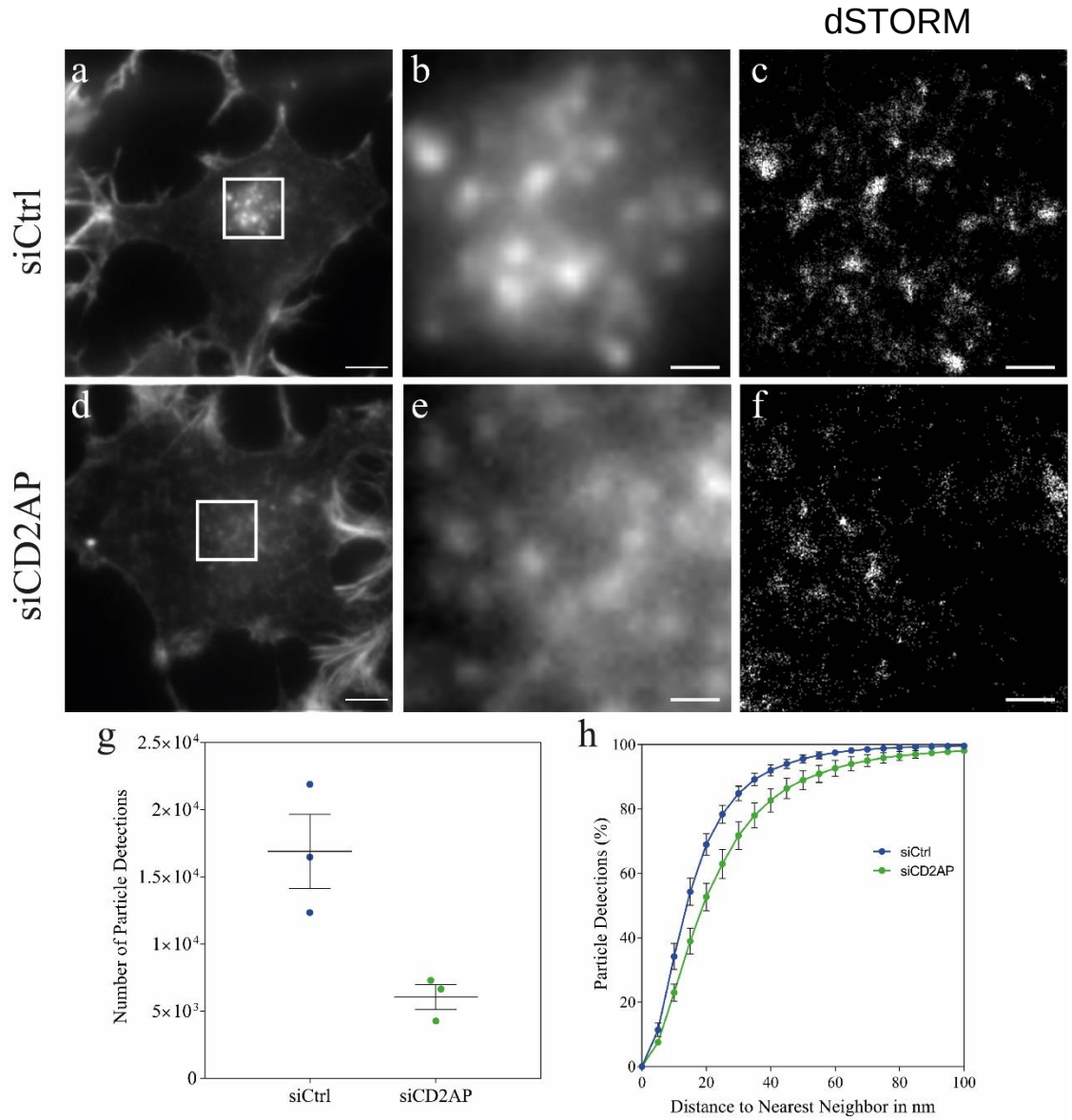

Figure 3.10 - CD2AP influences F-actin quantities and organization in the perinuclear region. **a), d)** Representative images of N2a cells labeled for F-actin in Control and in the absence of CD2AP, respectively. **b), e)** are, respectively, the white frame magnifications of a) and d). **c), f)** dSTORM images of b) and e). **g)** Shows quantity measurement, represented as the number of dSTORM detections. **h)** Shows nearest neighbor analysis being averaged between the cells analyzed for each condition. Scale bars **a, d** 5 µm. Scale bars **b, c, e, f** 1 µm.

To understand if endosomal F-actin is affected in the absence of CD2AP we analyzed the dSTORM F-actin detections in the area of influence of early endosomes. This area of influence was defined using a threshold as function of each endosome radius, meaning that bigger endosomes will have a bigger threshold. In the previous section we fixed the radius of the endosomal area of influence at 50 nm because we were comparing different types of endosomes with different size distributions. Now, because all endosomes are of the same type, the size distribution should be approximately the same and we used it as our variable to the area of influence.

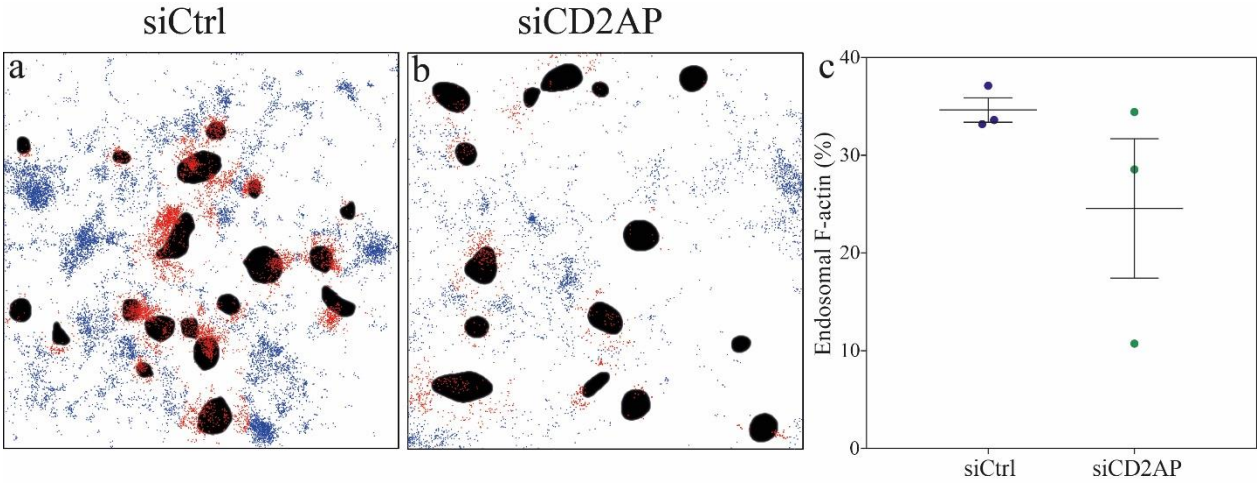

Figure 3.11 - Absence of CD2AP reduces endosomal F-Actin. **a), b)** Representation of endosomal F-actin in control and in the absence of CD2AP, respectively. Red represents F-actin associated with endosomes. The threshold for considering a part of endosomal F-actin is a function of endosomal size. Blue is F-actin not belonging to endosomes. Black represents endosomes. **c)** Percentage of total F-actin present in the ROI that considered endosomal F-actin.

We found that CD2AP KD cells have less F-actin in early endosome surroundings when comparing with control conditions (**Figures 3.11 a, b**). In control conditions the endosomal F-actin corresponds on average to 34 % of all F-actin present in this region (**Figures 3.11 c**). On the other hand, in CD2AP KD cells, there is a decrease of 29 % in the mean endosomal F-actin. We observed a variability in the fraction of endosomal F-actin in CD2AP KD cells which might be a consequence of a variable depletion of CD2AP or in a higher variability in the organization of the endosomal F-actin pool. When computing absolute F-actin counts (**Figure 3.12**), we observed that in CD2AP KD cells there is a mean decrease of 69 % of endosomal F-actin, suggesting that the polymerization of F-actin occurring at early endosomes is impaired in CD2AP KD cells as already observed in *Gauthier et al., 2007* [18]. Also, from previous results of our lab, we know that there is a significant decrease in the intensity of F-actin puncta associated with early endosomes corroborating this analysis.

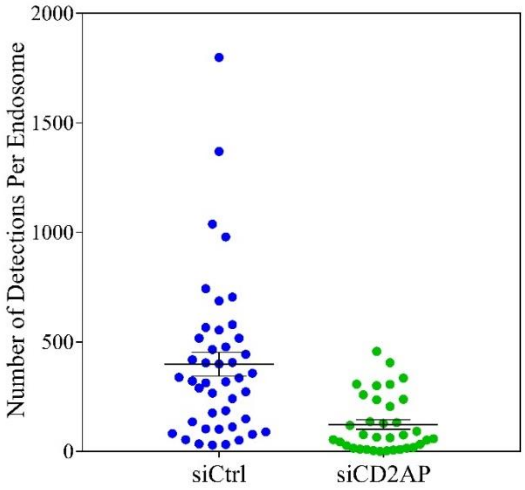

Figure 3.12 - Effect of the absence of CD2AP in absolute counts of F-actin detections per endosome.

Next we performed cluster analysis following the protocol described in **Appendix C**. Again, this analysis had the purpose of identifying the clusters and to segment them. After calculating the input parameters of the cluster algorithm, we obtained the cluster patterns of both conditions as illustrated in **Figures 3.13 c and f.**

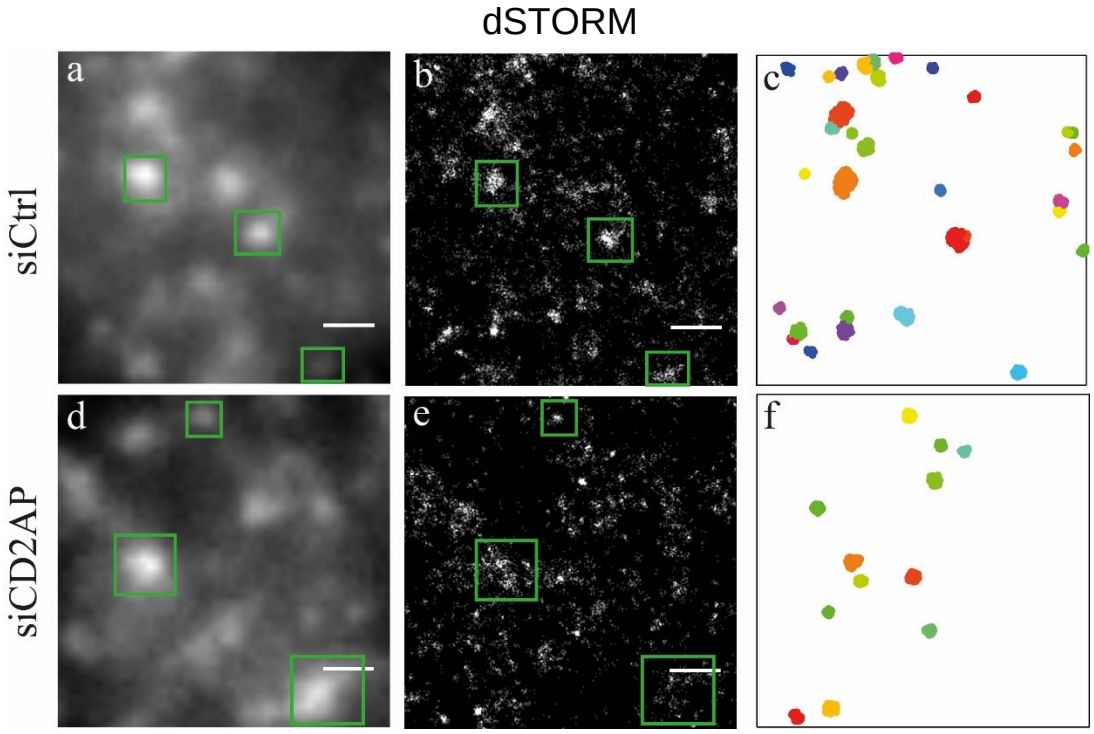

Figure 3.13 - dSTORM super resolution images reveal organization of diffraction limited F-actin puncta. **a), d)** Representative epifluorescence images of N2a cells labeled for F-Actin and transfected with non-targeting siRNA (a) and siRNA against CD2AP (d). **b), e)** dSTORM reconstructions of a) and d), respectively. **c), f)** representation of DBSCAN F-actin cluster identification of b) and e), respectively. Scale bars **a, d** 1 µm.

First of all, we compared the F-actin puncta in epifluorescence images (green boxes, **Figures 3.13 a and d**) with dSTORM reconstructions (green boxes, **Figures 3.13 b and e**) and observed that almost all epifluorescence puncta corresponded to dSTORM clusters in control cells while in CD2AP KD cells the epifluorescence F-actin puncta often corresponded to unclustered or small F-actin clusters structures (**Figures 3.13 d and e**), Quantification and plot of the number of clusters as well as the number of particles per cluster showed a decrease of 77 % in the mean number of clusters (**Figure 3.14 a**) and of 48 % in the mean number of F-actin detections per cluster (**Figure 3.14 b**) when comparing CD2AP KD cells to control conditions. The decrease in the number of clusters corroborates the results from the nearest neighbor analysis (**Figure 3.10 h**) because if the particles are more scattered then the DBSCAN density requisites are not so often fulfilled and there will be less clusters.

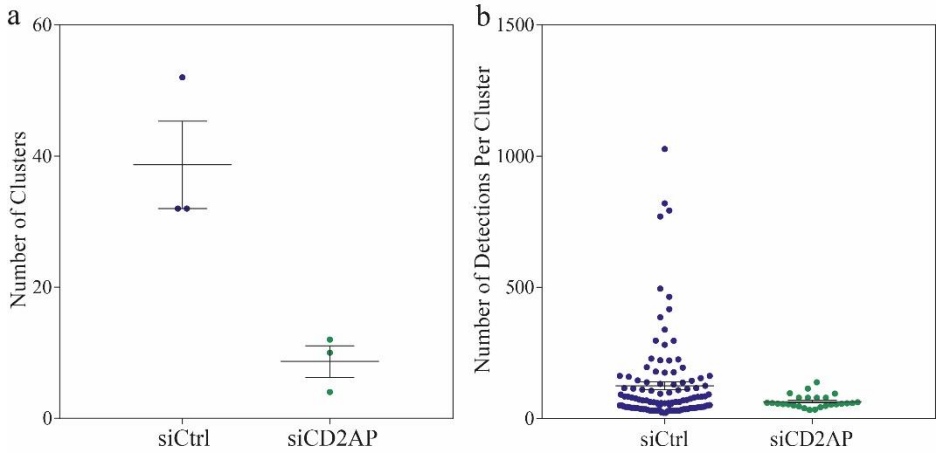

Figure 3.14 – Cluster Analysis in CD2AP KD cells. **a)** Number of Clusters per ROI per condition. **b)** Number of F-actin detections per Cluster.

We also calculated the fraction of clustered F-actin (**Figures 3.15 a-c**). This is a useful measurement because it can translate the capacity of F-actin assembly/stabilization and can be used in future studies that include proteins responsible for actin dynamics, cytoskeleton organization and regulation. We found a 69% reduction in clustered F-actin further supporting that upon CD2AP KD F-actin assembly/stability decreases (**Figure 3.15 c**). When looking at the number of F-actin detections we pointed the lack of cortactin recruitment caused by the absence of CD2AP as a possible reason for the decrease in polymerization activity and therefore for the decrease in F-actin detections. When looking to clustering activity, one possible explanation for the decrease in number of F-actin clusters, detections per cluster and fraction clustered might be the lack of activity of CP, known to stabilize dense F-actin networks by keeping the filaments short but stimulating the growth of new filaments. CP is not normally recruited in the absence of CD2AP and that might explain low clustering ability [14].

Previous analysis made in our lab using conventional fluorescence microscopy indicated that the percentage of early endosomes showing F-actin puncta colocalization decreased very slightly in the absence of CD2AP. In contrast, the cluster analysis based on dSTORM detections indicated that CD2AP KD cells had a 83 % decrease in the mean percentage of early endosomes in the perinuclear region with

colocalizing F-actin clusters (**Figures 3.15 d-f**). First of all, apparent colocalization of F-actin puncta with endosomes in conventional epifluorescence imaging can be refuted by using dSTORM as was already discussed in **section 3.1** (**Figures 3.1 g-h**). Second, the wide-field F-actin puncta taken as clusters can be dismantled after dSTORM reconstruction into more than one cluster or in no cluster at all (might not fulfill density requisites). Nevertheless, we need to increase our sample before being able to confirm this tendency.

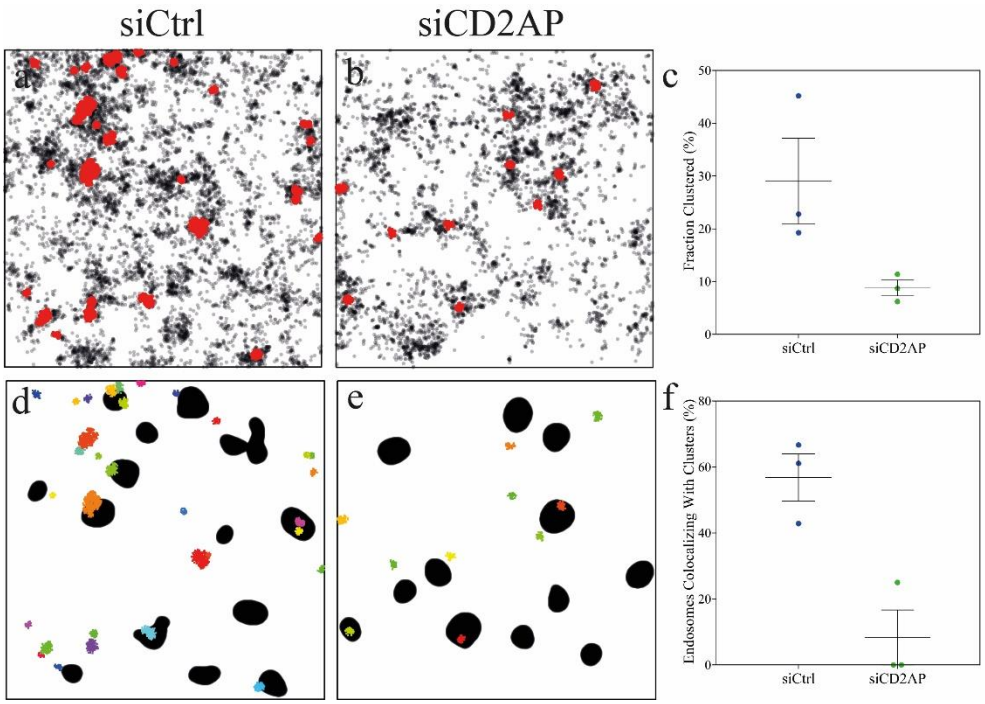

Figure 3.15 - F-Actin exhibits limited clustering assembly and a decrease in cluster colocalization with early endosomes without CD2AP. **a), b)** Clusters with and without CD2AP, respectively. Red indicates clusters and black dots are detections not belonging to any cluster identified by DBSCAN. **c)** Quantification of the percentage belonging to a cluster for both conditions. **d), e)** Cluster colocalization with endosomes. Color aggregates represent the clusters and black islands represent the endosomes. **f)** Percentage of endosomes with colocalizing clusters.

Overall, the results in this section seem to place CD2AP as a major perinuclear F-actin regulator, having a great influence not only in the assembly of F-actin into clusters but also in its the presence at early endosomes and in the perinuclear region in general.

3.5 F-Actin and CD2AP Mutant

After the identification of a rare mutation in CD2AP predicted to be deleterious in AD [97] we decided to investigate its impact in F-actin patterns using dSTORM. Previous results reported in the literature associate the C-terminal of the CD2AP protein to interact with F-actin and necessary to form F-actin structures at the cytoplasm and in early endosomes [18]. In order to be able to observe the effects that this particular mutation has on the perinuclear F-actin patterns we transfected cells with specific DNA plasmids encoding CD2AP Wild Type (WT), the mutant form tagged with GFP (MUT) and a vector expressing GFP

as control (GFP). GFP fluorescence signal was used to identify the transfected cells. We labeled F-actin and early endosomes following the same protocol as in **section 3.3**.

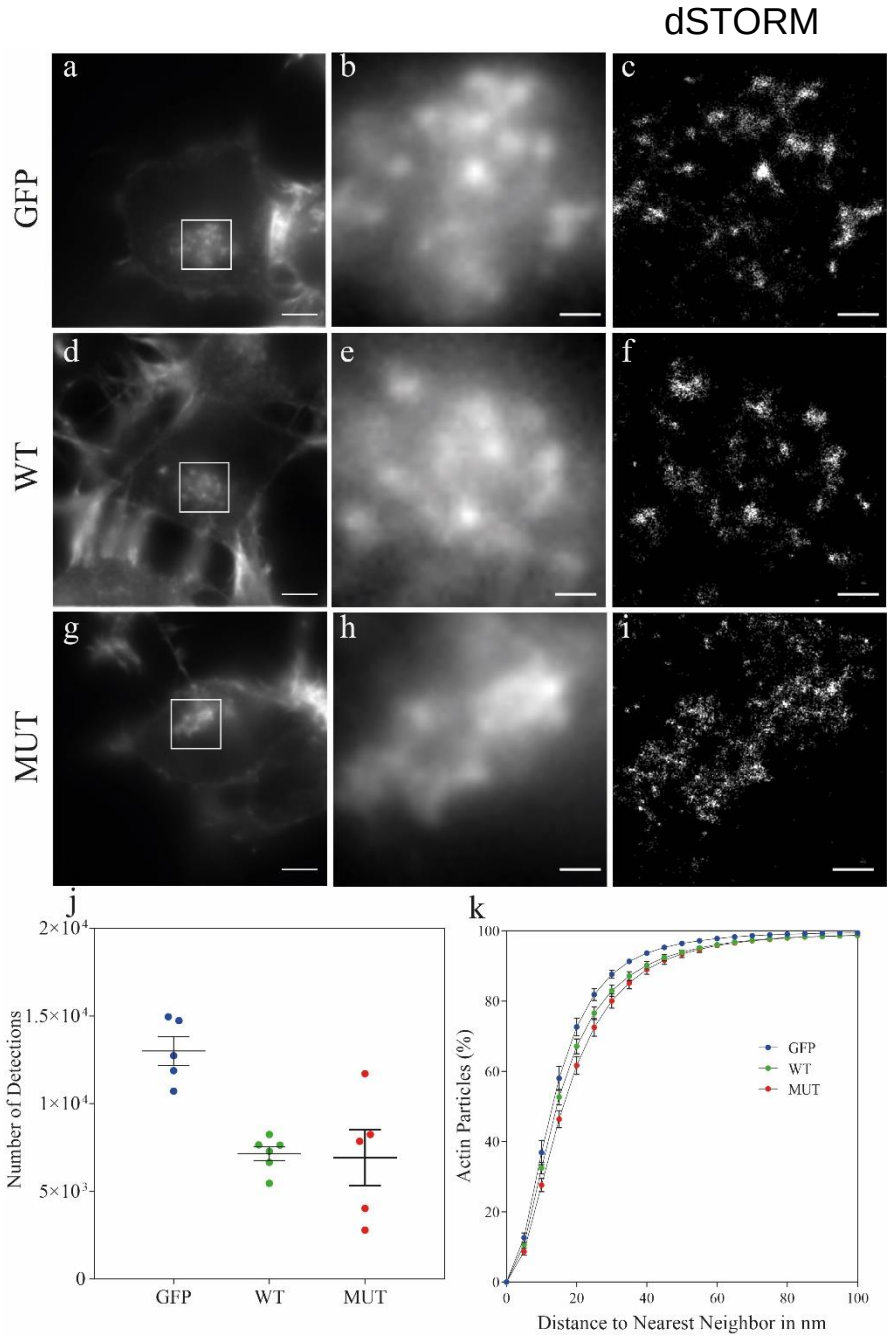

Figure 3.16 - Perinuclear F-Actin is altered when overexpressing Wild Type and Mutant CD2AP. **a), d), g)** Epifluorescence images of N2a cells stained against F-Actin in control, wild type and mutant conditions, respectively. **b), e), h)** white frames magnifications of a), d) and g) respectively. **c), f), i)** are dSTORM reconstructions of b), e) and h). **j)** F-Actin dSTORM detections in the perinuclear region. **k)** Cumulative Nearest neighbor distances in percentage of total F-actin detected in this region. Scale bars **a, d, g** 5 µm. Scale bars **b, e, h, c, f, i** 1 µm.

Figures 3.16 a-i shows the perinuclear F-actin in all experimental conditions. Both control and Wild Type conditions (**Figures 3.16 a-f**) exhibited similar F-actin puncta as visualized by epifluorescence and

similar F-actin clusters as visualized in dSTORM reconstructions. In CD2AP mutant cells, the F-actin pattern appeared more scattered in opposition to the big clusters and compact structures detected in control and Wild-Type conditions (**Figures 3.16 g-i**). Interestingly, when analyzing the number of F-actin detections (**Figure 3.16 j**), we detected a 45 % mean decrease of F-actin detections in cells expressing wild-type and mutant CD2AP compared to control cells. The decrease in wild type conditions suggests that an excess of CD2AP disturbs F-actin polymerization and with these results we have no evidences that the mutation affects the F-actin polymerization in a different way. Besides that, with these results we could hypothesize that there is more than one mechanism through which CD2AP affects F-actin polymerization since interaction with cortactin should not be affected neither in Wild Type and Mutant forms. In addition, the nearest neighbor curves (**Figure 3.16 k**) confirmed a gradual decrease in the patterns compactness, indicating that both the wild type and the mutation are altering F-actin stabilization.

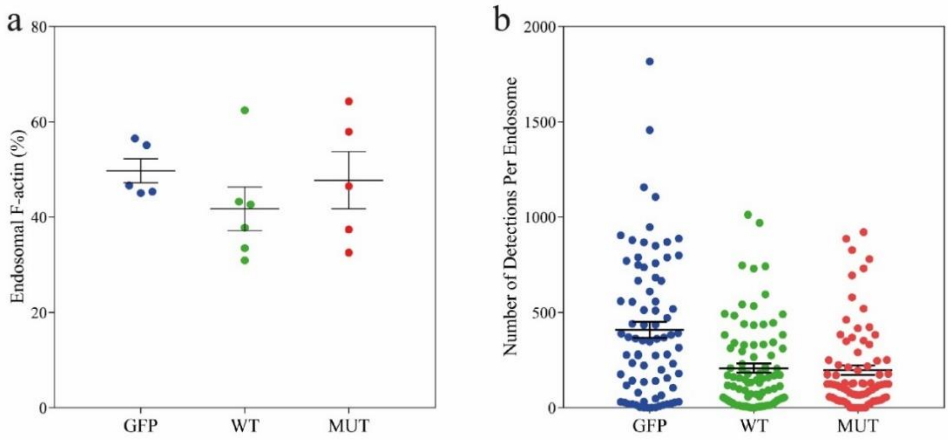

Figure 3.17 - Endosomal F-Actin is similar when comparing overexpression of Wild Type and Mutant CD2AP. **a), b)** Percentage of endosomal F-Actin and Absolute F-Actin dSTORM detections within endosomal distance threshold.

When overexpressing wild type and mutant CD2AP we noted that the average endosomal F-actin percentage decreased 16 % and 4 %, respectively, compared with control conditions (**Figure 3.17 a**). In contrast, we observed a steeper decrease in the absolute count of detections per endosome of nearly 50% for both wild-type and mutant CD2AP (**Figure 3.17 b**). The lack of difference between Wild-Type and Mutant form of CD2AP suggests that the mutation has an effect similar of having an excess of healthy protein in the F-actin polymerization at early endosomes.

We also did a cluster analysis (**Figures 3.18 c, f, i**) and found an important 52 % mean decrease of F-actin clusters in CD2AP mutant cells while observing a 38 % decrease in CD2AP wild-type cells. Additionally, the absolute number of F-actin detections in each cluster was more reduced in CD2AP mutant (56 %) than in wild-type cells (38 %) in comparison with control cells. We observed a larger variability in the number of clusters of the mutant condition which may be consequence of the also variable number of F-actin detections (**Figure 3.16 j**) or because of different quantities of mutant protein expressed between cells.

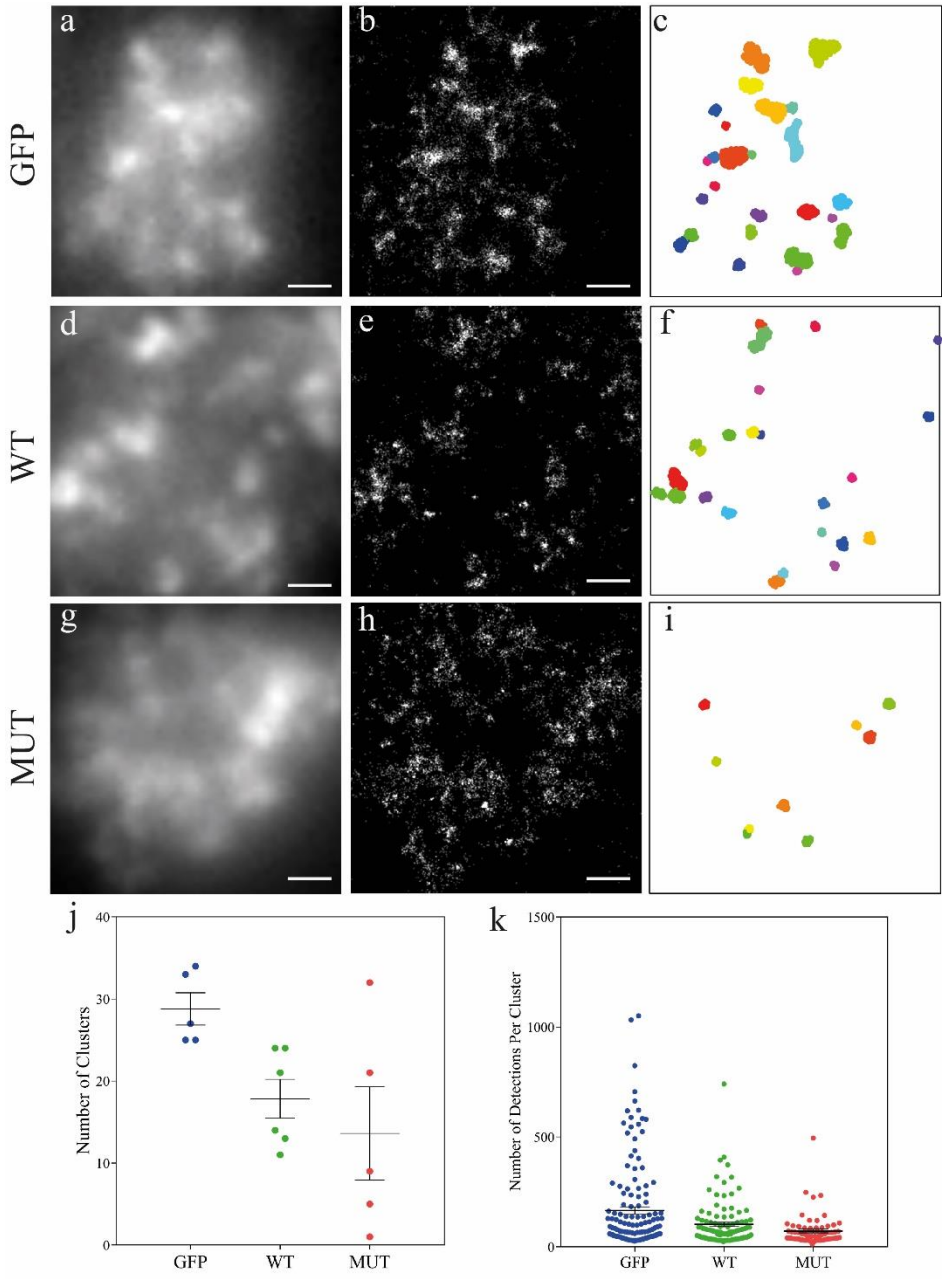

Figure 3.18 - Cluster analysis overexpressing Wild Type and Mutant CD2AP. **a), d), g)** Representative epifluorescence images labeled against F-Actin in control, wild type and mutant overexpression, respectively. **b), e), h)** dSTORM reconstruction of a), d) and g) respectively. **c), f), i)** DBSCAN cluster identification of b), e) and h), respectively. The input parameters are k = 30 and ε = 60 nm. **j)** Number of identified clusters per condition. **k)** Number of dSTORM F-Actin detections per cluster. Scale bars 1 µm.

Finally, we determined the percentage of clustered F-actin (**Figures 3.19 a-c**) and inspected their colocalization with early endosomes (**Figures 3.19 d-f**). In wild type conditions there was a 29% reduction in clustered F-actin and a 28 % reduction in colocalization with early endosomes. Differently in CD2AP mutant cells the F-actin pattern exhibited a more important 67 % reduction in the percentage of clustered F-actin and a similar 51% reduction in the colocalization of these F-actin clusters with early endosomes.

Our cluster analysis showed dissimilarities between the Wild Type and Mutant forms. The decrease observed in the mutant conditions suggests that the mutation at the actin binding site of CD2AP might have great influence in the formation and stabilization of F-actin clusters in N2a cells (**Figure 3.19 g**). Additionally, F-actin structure formation at early endosomes is also greatly decreased in this condition (**Figure 3.19 h**).

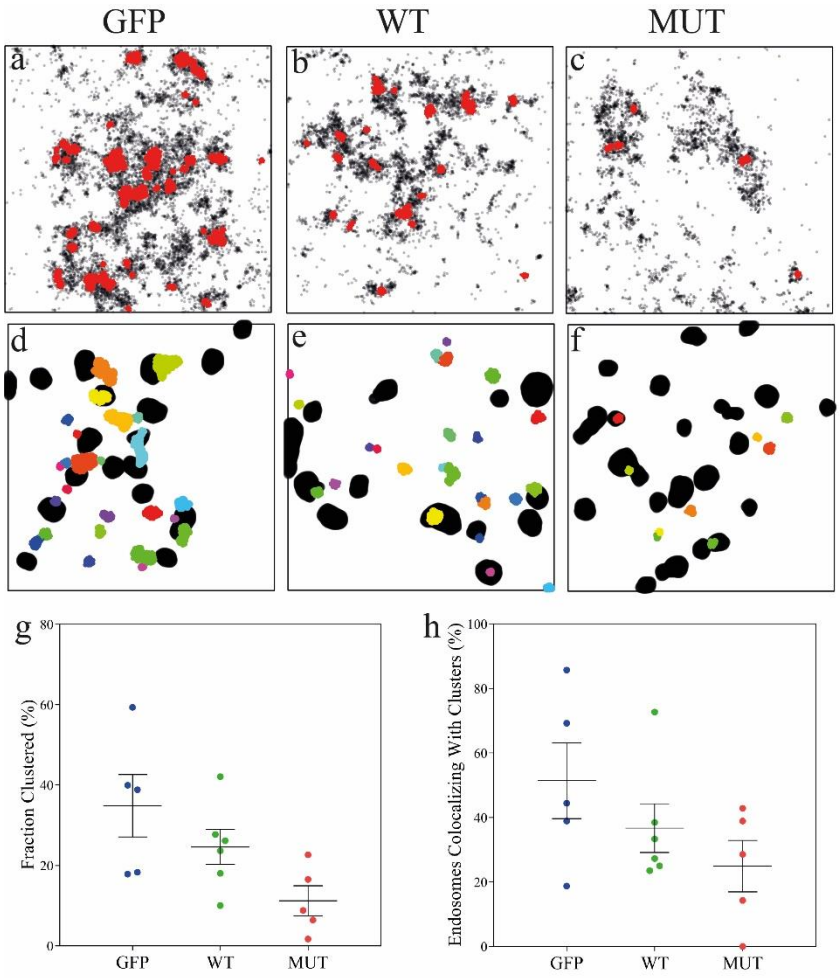

Figure 3.19 - Wild Type and Mutant CD2AP overexpression affect cluster assembly and its colocalization with early endosomes. **a)**, **b), c)** Representation of F-Actin in cluster and non-cluster form in control, wild type and mutant overexpression, respectively. Red agglomerates are clusters identified by DBSCAN with input parameters k -= 30 and ε = 60 nm. Black dots are DBSCAN noise points. **d), e), f)** Representative F-Actin cluster (color agglomerates) colocalization with early endosomes (black islands) in control, wild type and mutant overexpression, respectively. **g)** Percentage of total F-Actin dSTORM detections per cell that belong to a cluster. **h)** Percentage of early endosomes per cell that have a colocalizing cluster.

In this experiment we observed a similar negative behavior between wild type and mutant conditions in the amount of F-actin in the perinuclear region and polymerization at early endosomes. Interestingly, different results were obtained in the cluster analysis between both conditions, suggesting a negative role of this particular mutation in F-actin cluster formation and stabilization. Wild type also had a lighter negative effect indicating another mechanism through which an excess of CD2AP also impacts F-actin clusters.

4 Conclusion and Future Trends

The objective of this work was to apply dSTORM in the study of intracellular traffic, more specifically, in studying F-actin patterns and their relation with early endosomes as a function of CD2AP, a protein expressed by a gene known to be altered in AD. In order to accomplish that, our work was divided into two major parts.

In the first part, we explored the super resolution technique and applied procedures essential to our analysis. We planned to use the mapping capabilities of dSTORM to observe the distribution of F-actin in the perinuclear region. In order to be able to trust in our localizations the probe used to label F-actin was phalloidin conjugated with Alexa Fluor 647 combined with an imaging buffer known to give excellent performs to this fluorophore. With this probe we also ensured that the labeling had a high affinity with F-actin and the size of the structure was not significantly increased. The fluorophore is described as one of the top performers, giving the localization algorithms a bright enough signal to determine the localization with high precision. Our measurements had, on average, a localization precision of 20 nm which is within previous reports using dSTORM analysis. We also corrected artifacts coming from the photophysical behavior of the fluorophores by: a) implementing filters to our detected population based on parameters given by the localization algorithms; b) applying a merging algorithm, eliminating consecutive detections of the same fluorophore, that is critical when performing quantitative analysis in SMLM methods. However, it still remains a challenge to correct for detections coming from the same fluorophore that are separated in time.

In the second part we aimed to understand if F-actin could be implicated in CD2AP dependent beta amyloid production at early endosomes. We started by finding out if perinuclear F-actin is located more towards early endosomes than late endosomes by accessing dSTORM F-actin detection locations and mapping them against endosomes. Our results point in the direction that this perinuclear F-actin might be more present at early endosomes and thus could be essential to endosomal sorting events such as the ones necessary for beta-amyloid production.

After, we compared the F-actin patterns in control cells with cells with CD2AP KD. From the results, summarized in **Table E.1** we found that: A) F-actin levels in the perinuclear region decreased based on the number of dSTORM detections; B) The compactness of the F-actin pattern, analyzed by measuring the nearest neighbor (NN) distance to each particle, decreased in CD2AP KD cells; C) Less early endosomal F-actin; D) The clustering of F-actin was greatly decreased, with the percentage of the total F-actin pattern belonging to clusters was 70 % reduced and the few existent clusters had less particles. We detected a very small percentage of early endosomes colocalizing with F-actin clusters indicating that clustering of perinuclear actin is controlled at early endosomes by CD2AP.

Finally, we found that an AD mutation in CD2AP alters the F-actin patterns. Overall we observed similarities between CD2AP KD cells and mutant CD2AP expressing cells, especially when comparing the number of detections, number of clusters, fraction clustered and detections per cluster. Indeed, the mutant form of CD2AP seems to affect the F-actin clustering capabilities by controlling its polymerization and stabilization (**Table E.2**). However, there was lot of variability in the mutant conditions, thus we need a larger

sample size to draw conclusions. CD2AP wild type overexpression led to an intermediate standing in our measurements, suggesting that an excess of CD2AP also compromises the normal F-actin dynamics.

Cell biology is known for being a field with a lot of variability because the cell is a very complex system and upon treatments or even in cell culture procedures the resultant population of cells shows a lot of variability due to metabolic or cell cycle status. dSTORM also has a lot of variability with analysis involving molecule counting. We need to further increase the number of experiments to reduce our overall variability but also to validate the results by other means. For example, in this work we implemented a clustering algorithm, DBSCAN. DBSCAN is used when the clusters have arbitrary shapes and with points not belonging to any cluster, characteristics that fit our data. It also facilitated the analysis output by integration in R, through an available package. However, without any biological reason for the input parameters due to the lack of characterization of these F-actin patterns in the literature, we had to adopt an empirical protocol to find them, which may not be that precise. In the future, analysis could be performed by other cluster algorithms like the one presented by *Levet et al, 2015* [98] or *Andronov et al*., 2016 [99], based on tessellation segmentation. This means that individual polygons are centered on each molecule, creating an area of influence with geometrical properties (morphometric parameters such as shape, surface area, and eccentricity) that allow more precise methods for cluster identification.

We should also perform endosomal super resolution in order to reduce associated errors coming from the fact that we used conventional epifluorescence to segment endosomes. As already discussed for actin, the endosome objects may be bigger than they actually are, due to the resolution limitations of epifluorescence. In this work we did not performed endosomal super resolution because of time restrains since it requires some extent of optimization, both in labeling, acquisition and analysis thus we opted to optimize F-actin first.

Actin is very dynamic in intracellular processes. Its own nature is to be continuously polymerized, depolymerized and stabilized as a function of many actin binding proteins. With the imaging of fixed cells we lose a lot of information. So, in the future we want to be able to apply live cell imaging to better understand the role of CD2AP in endosomal actin dynamics. More specifically, we want to apply live super resolution based on radial fluctuations [100].

Another important experiments will be to investigate the flat clathrin pool associated with early endosomes whose cargo is going to follow for degradation. First of all it will be interesting to see through dSTORM super resolution if endosomal F-actin colocalizes with endosomal clathrin has it colocalizes with the clathrin present at the plasma membrane where it is known to have a role in endocytosis by supplying the force necessary to complete endocytic vesicle formation [30–35]. From there on, connections between Hrs, ESCRT complexes and ubiquitin will be studied as they are crucial in invagination processes [41,101–103], still not well understood that could help explain APP trapping at early endosomes membrane. Cortactin and capping protein will be investigated as function of CD2AP through conventional fluorescence microscopy with the objective of establishing a possible explanation for the decreasing of perinuclear F-actin levels. Finally, to reduce the variability of the mutant results, we will repeat the measurements experiment but altering the cell culture protocol by knocking down completely the CD2AP in the cell and then expressing the mutant form to eliminate the mixture of healthy and mutant protein.

Bibliography

1. Alzheimer's Association. *2017 Alzheimer's Disease Facts and Figures*. **13**, 325-373 (2017).
2. Huang, Y. & Mucke, L. Review Alzheimer Mechanisms and Therapeutic Strategies. *Cell* **148,** 1204–1222 (2012).
3. Bekris, L. M. et al. Genetics of Alzheimer Disease. *J Geriatr Psychiatry Neurol.* **23,** 213–227 (2010).
4. Lister Hill National Center for Biomedical Communications; U.S. National Library of Medicine;National Institutes of Health;Department of Health & Human Services. *APOE Gene*. (2017).
5. Li, Hao; Wetten, Sally; Li, L. et el. Candidate Single-Nucleotide Polymorphisms From a Genomewide Association Study of Alzheimer Disease. *Arch Neurol.* **65,** 45–53 (2008).
6. Coon, K. D. et al. A High-Density Whole-Genome Association Study Reveals That APOE Is the Major Susceptibility Gene for Sporadic Late-Onset. *J. Clin. Psychiatry* **68,** 613–618 (2007).
7. Grupe, A. et al. Evidence for novel susceptibility genes for late-onset Alzheimer's disease from a genome-wide association study of putative functional variants. *Hum. Mol. Genet.* **16,** 865–873 (2007).
8. Lambert, J.-C. et al. Meta-analysis of 74,046 individuals identifies 11 new susceptibility loci for Alzheimer's disease. *Nat. Genet.* **45,** 1452–1458 (2013).
9. Hollingworth, P. et al. Common variants in ABCA7 , MS4A6A / MS4A4E , EPHA1 , CD33 and CD2AP are associated with Alzheimer's disease. *Nat Genet.* **43,** 429–435 (2011).
10. Naj, A. C. et al. Common variants in MS4A4/MS4A6E, CD2uAP, CD33, and EPHA1 are associated with late-onset Alzheimer's disease. *Nat Genet.* **43,** 436–441 (2011).
11. Dustin, M. L. *et al.* A Novel Adaptor Protein Orchestrates Receptor Patterning and Cytoskeletal Polarity in T-Cell Contacts. *Cell* **94,** 667–677 (1998).
12. Cormont, M. *et al.* CD2AP / CMS Regulates Endosome Morphology and Traffic to the Degradative Pathway Through its Interaction with Rab4 and c-Cbl. *Traffic* **4,** 97–112 (2003).
13. Lynch, Danielle K.; Winata, Stephanie C.; Lyons, R. J. et al. A Cortactin-CD2-associated Protein (CD2AP) Complex Provides a Novel Link between Epidermal Growth Factor Receptor Endocytosis and the Actin Cytoskeleton. *J. Biol. Chem.* **278,** 21805–21813 (2003).
14. Zhao, J. *et al.* CD2AP Links Cortactin and Capping Protein at the Cell Periphery To Facilitate Formation of Lamellipodia. *Mol. Cell. Biol.* **33,** 38–47 (2013).
15. Lehtonen, S., Zhao, F. & Lehtonen, E. CD2-associated protein directly interacts with the actin cytoskeleton. *Am J Physiol Ren. Physiol* **283,** F734–F743 (2002).
16. Bruck, S. *et al.* Identification of a Novel Inhibitory Actin-capping Protein Binding Motif in CD2-associated Protein. *J Biol Chem* **281,** 19196–19203 (2006).
17. Welsch, T. *et al.* Association of CD2AP with dynamic actin on vesicles in podocytes. *Am J Physiol Ren. Physiol* **289,** 1134–1143 (2005).
18. Gauthier, N. C. *et al.* Early endosomes associated with dynamic F-actin structures are required for

late traffi cking of H. pylori VacA toxin. *J. Cell Biol.* **177,** 343–354 (2007).

19. Kobayashi, S., Sawano, A., Nojima, Y., Shibuya, M. & Maru, Y. The c-Cbl/CD2AP complex regulates VEGF-induced endocytosis and degradation of Flt-1 (VEGFR-1). *FASEB J.* **1,** (2004).
20. Dominguez, R. & Holmes, K. C. Actin Structure and Function. *Annu. Rev. Biophys.* **40,** 169–186 (2011).
21. Winder, S. J. . & Ayscough, K. R. Actin-binding proteins. *J. Cell Sci.* **118,** 651–654 (2005).
22. Lodish H, Berk A; Zipursky SL, et al. *The Dynamics of Actin Assembly. Molecular Cell Biology* (2000).
23. Pollard, T. D. & Borisy, G. G. Cellular Motility Driven by Assembly and Disassembly of Actin Filaments. *Cell* **112,** 453–465 (2003).
24. Desmarais, V., Macaluso, F., Condeelis, J. & Bailly, M. Synergistic interaction between the Arp2 / 3 complex and cofilin drives stimulated lamellipod extension. *J. Cell Sci.* **117,** 3499–3510 (2004).
25. Pant, K., Chereau, D., Hatch, V., Dominguez, R. & Lehman, W. Cortactin Binding to F-actin Revealed by Electron Microscopy and 3D Reconstruction. *J. Mol. Biol* **359,** 840–847 (2006).
26. Weed, S. A. *et al.* Cortactin Localization to Sites of Actin Assembly in Lamellipodia Requires Interactions with F-Actin and the Arp2 / 3 Complex. *J. Cell. Biol* **151,** 29–40 (2000).
27. Gautreau, A. & Derivery, E. Actin Polymerization Controls the Organization of WASH Domains at the Surface of Endosomes. *PLoS One* **7,** e39774 (2012).
28. Edwards, M. *et al.* Capping protein regulators fine-tune actin assembly dynamics. *Nature Reviews Molecular Cell Biology* **15,** 677-689 (2014).
29. Wegner, A. & Isenbergt, G. 12-Fold difference between the critical monomer concentrations of the two ends of actin filaments in physiological salt conditions. *Proc. Nati Acad. Sci. USA* **80,** 4922–4925 (1983).
30. Mcmahon, H. T. & Boucrot, E. Molecular mechanism and physiological functions of clathrin - mediated endocytosis. *Nat. Rev. Mol. Cell Biol.* **12,** 517–533 (2011).
31. Merrifield, C. J., Feldman, M. E., Wan, L. & Almers, W. Imaging actin and dynamin recruitment during invagination of single clathrin-coated pits. *Nat. Cell Biol.* **4,** 691–698 (2002).
32. Merrifield, C. J., Perrais, D., Zenisek, D., Saëns, S. & Cedex, B. Coupling between Clathrin-Coated-Pit Invagination , Cortactin Recruitment , and Membrane Scission Observed in Live Cells. *Cell* **121,** 593–606 (2005).
33. Yarar, D., Waterman-storer, C. M. & Schmid, S. L. A Dynamic Actin Cytoskeleton Functions at Multiple Stages of Clathrin-mediated Endocytosis □. *Mol. Biol. Cell* **16,** 964–975 (2005).
34. Drubin, D. G. Actin assembly and endocytosis: From Yeast to Mammals. *Annu. Rev. Cell Dev. Biol.* **19,** 287–332 (2003).
35. Merrifield, C. J. Seeing is believing : imaging actin dynamics at single sites of endocytosis. *Trends Cell Biol.* **14,** (2004).
36. Gautreau, A., Oguievetskaia, K. & Ungermann, C. Function and Regulation of the Endosomal Fusion and Fission Machineries. *Cold Spring Harb Perspect Biol* **6,** 1–16 (2014).

37. Huotari, J. & Helenius, A. Endosome maturation. *EMBO J.* **30,** 3481–3500 (2011).
38. Derivery, E. et al. Article The Arp2 / 3 Activator WASH Controls the Fission of Endosomes through a Large Multiprotein Complex. *Dev. Cell* **17,** 712–723 (2009).
39. Gomez, T. S. & Billadeau, D. D. Article A FAM21-Containing WASH Complex Regulates Retromer-Dependent Sorting. *Dev. Cell* **17,** 699–711 (2009).
40. Pickart, C. M. & Eddins, M. J. Ubiquitin : structures , functions , mechanisms. *Biochim. Biophys. Acta - Mol. Cell Res.* **1695,** 55–72 (2004).
41. Raiborg, C. *et al.* Hrs sorts ubiquitinated proteins into clathrin-coated microdomains of early endosomes. *Nat. Cell Biol.* **4,** 394–398 (2002).
42. Jovic, Marko; Sharma, M. et al. The early endosome: a busy sorting station for proteins at the crossroads. *Histol Histopathol.* **25,** 99–112 (2010).
43. Calabia-linares, C. *et al.* Endosomal clathrin drives actin accumulation at the immunological synapse. *J. Cell Sci.* **124,** 820–830 (2011).
44. O'Brien, Richard J.; Wong, P. C. Amyloid Precursor Protein Processing and Alzheimer's Disease. *Annu Rev Neurosci.* **34,** 185–204 (2011).
45. Hartmann, T. et al. Distinct sites of intracellular production for Alzheimer's disease Aβ40/42 amyloid peptides. *Nat. Med.* **3,** 1016–1020 (1997).
46. Xu, H. et al. Generation of Alzheimer β-amyloid protein in the trans-Golgi network in the apparent absence of vesicle formation. *PNAS* **94,** 3748–3752 (1997).
47. Hecler, F. R. C., Isodia, S. A. S. S., Reengard, P. A. U. L. G. & Uaxi, H. X. U. Endoplasmic reticulum and trans-Golgi network generate distinct populations of Alzheimer ␣ -amyloid peptides. *PNAS* **96,** 742–747 (1999).
48. Furukawa, K. *et al.* Increased Activity-Regulating and Neuroprotective Efficacy of a-Secretase-Derived Secreted Amyloid Precursor Protein Conferred by a C-Terminal Heparin-Binding Domain. *J. Neurochem.* **67,** 1882–1896 (1996).
49. Sisodia, S. S. precursor protein cleavage by a membrane- bound protease. *PNAS* **89,** 6075–6079 (1992).
50. Cai, H. *et al.* BACE1 is the major β -secretase for generation of A β peptides by neurons. *Nat. Neurosci.* **4,** 233–234 (2001).
51. Vassar, R. et al. β-Secretase Cleavage of Alzheimer's Amyloid Precursor Protein by the Transmembrane Aspartic Protease BACE. *Science (80-.).* **286,** 735–741 (1999).
52. Zhang, Y., Thompson, R., Zhang, H. & Xu, H. APP processing in Alzheimer ' s disease. *Mol. Brain* **4,** 3 (2011).
53. Das, U. *et al.* Activity-induced convergence of APP and BACE-1 in acidic microdomains via an endocytosis-dependent pathway. *Neuron* **79,** 447–460 (2014).
54. Hong, W. *et al.* Amyloid precursor protein traffics from the Golgi directly to early endosomes in an Arl5b- and AP4-dependent pathway. *Traffic* **18,** 159–175 (2017).

55. Zhi, P. *et al.* Intracellular Itinerary of Internalised β -Secretase , BACE1 , and Its Potential Impact on β -Amyloid Peptide Biogenesis. *Traffic* **14,** 997–1013 (2013).
56. Sannerud, R. *et al.* precursor protein (APP) processing by mediating the endosomal sorting of BACE1 β. *PNAS* **108,** E559–E568 (2011).
57. Haass, C. et al. Amyloid β-peptide is produced by cultured cells during normal metabolism. *Nature* **359,** 322–325 (1992).
58. Morel, E. *et al.* Phosphatidylinositol-3-phosphate regulates sorting and processing of amyloid precursor protein through the endosomal system. *Nat. Commun.* **4,** 1–13 (2013).
59. Edgar, J. R., Wille, K., Gouras, G. K. & Futter, C. E. ESCRTs regulate amyloid precursor protein sorting in multivesicular bodies and intracellular amyloid- β accumulation. *J Cell Sci* **128,** 2520–2528 (2015).
60. Ubelmann, F. et al. Bin 1 and CD 2 AP polarise the endocytic generation of beta-amyloid. *EMBO Rep.* **18,** 102–122 (2017).
61. Sanderson, Michael J. et al. Fluorescence Microscopy. *Cold Spring Harbor protocols*.**10** (2014).
62. Verdaasdonk, J. S. et al. Bending the Rules: Widefield Microscopy and the Abbe Limit of Resolution. *J Cell Physiol.* **229,** 132–138 (2014).
63. Ovesny, M., Computational methods in single molecule localization microscopy., PhD thesis, Charles University, Prague (2016).
64. Utah, U. of. Super-Resolution Microscopy Tutorial. (2011). Available at: http://advanced-microscopy.utah.edu/education/super-res/. (Accessed: 6th December 2017)
65. Rust, Michael J.; Bates, Mark; Zhuang, X. Stochastic optical reconstruction microscopy (STORM) provides sub-diffraction-limit image resolution. *Nat Methods* **3,** 793–795 (2006).
66. Schermelleh, L., Heintzmann, R. & Leonhardt, H. A guide to super-resolution fluorescence microscopy. *J. Cell Biol.* **190,** 165–175 (2010).
67. Prescher, J. Assembly and optimization of a super-resolution STORM microscope for nanoscopic imaging of biological structures. (2016).
68. Huang, B. et al. Super resolution fluorescence microscopy. *Annu Rev Biochem* **78,** 993–1016 (2009).
69. van de Linde, S. et al. Direct stochastic optical reconstruction microscopy with standard fluorescent probes. *Nat. Protoc.* **6,** 991–1009 (2011).
70. Dempsey, G. T., Vaughan, J. C., Chen, K. H., Bates, M. & Zhuang, X. Evaluation of fluorophores for optimal performance in localization-based super-resolution imaging. *Nat. Methods* **8,** (2011).
71. Ma, H et al., A simple and cost-effective setup for super-resolution localization microscopy. *Scientific Reports* **7,** 1542 (2017).
72. Diekmann, R. et al. Characterization of an industry- grade CMOS camera well suited for single molecule localization microscopy – high performance super-resolution at low cost. *Scientific Reports* **7,** 14425 (2017).
73. Leyton-Puig, D., Kedziora, K. M., Isogai, T., Broek, B. Van Den & Jalink, K. PFA fixation enables artifact-free super-resolution imaging of the actin cytoskeleton and associated proteins. *Co. Biol. Ltd*

5, 1001–1009 (2016).

74. Lehmann, M., Lichtner, G., Klenz, H. & Schmoranzer, J. Novel organic dyes for multicolor localization-based super-resolution microscopy. *J. Biophotonics* **9,** 161–170 (2016).
75. Edelstein, Arthur D; Tsuchida, Mark A; Amodaj, Nenad; Pinkard, Henry; Vale, Ronald D; Stuurman, N. Advanced methods of microscope control using μManager software. *J. Biol. Methods* **1,** (2014).
76. Ovesný, M.; Křížek, P.; Borkovec J.; Švindrych, Z.; Hagen, G. M. ThunderSTORM: a comprehensive ImageJ plugin for PALM and STORM data analysis and super-resolution imaging. *Bioinformatics* **30,** 2389–2390 (2014).
77. RStudio Team. RStudio: Integrated Development for R., RStudio Inc, Boston MA, (2016).
78. Lambert, T. J. & Waters, J. C. Navigating challenges in the application of superresolution microscopy. *J. Cell Biol.* 1–11 (2016).
79. Lo, A., Linde, S. Van De, Dabauvalle, M., Rieger, B. & Heilemann, M. Super-resolution imaging visualizes the eightfold symmetry of gp210 proteins around the nuclear pore complex and resolves the central channel with nanometer resolution. *J. Cell Sci.* **125,** 570–575 (2011).
80. Sauer, M. Localization microscopy coming of age : from concepts to biological impact. *J. Cell Sci.* **126,** 3505–3513 (2013).
81. Legant, W. R. *et al.* High-density three-dimensional localization microscopy across large volumes. *Nat. Methods* **13,** 359–365 (2016).
82. Nicovich, P. R., Owen, D. M. & Gaus, K. Turning single-molecule localization microscopy into a quantitative bioanalytical tool. *Nat. Protoc.* **12,** (2017).
83. Puchner, E. M., Walter, J. M., Kasper, R., Huang, B. & Lim, W. A. Counting molecules in single organelles with superresolution microscopy allows tracking of the endosome maturation trajectory. **110,** (2013).
84. Shivanandan, A., Deschout, H., Scarselli, M. & Radenovic, A. Challenges in quantitative single molecule localization microscopy. *FEBS Lett.* **588,** 3595–3602 (2014).
85. Mollazade, M. *et al.* Can single molecule localization microscopy be used to map closely spaced RGD nanodomains?. *PLoS One* **7,** 1–17 (2017).
86. Veatch, S. L. *et al.* Correlation Functions Quantify Super-Resolution Images and Estimate Apparent Clustering Due to Over-Counting. *PLoS One* **7,** (2012).
87. Coltharp, C., Kessler, R. P. & Xiao, J. Accurate Construction of Photoactivated Localization Microscopy (PALM) Images for Quantitative Measurements. *PLoS One* **7,** 1-15 (2012).
88. Ovesny, M. Guidelines for the choice of parameters. (2015). Available at: https://github.com/zitmen/thunderstorm/wiki/Guidelines-for-the-choice-of-parameters.
89. Huang, F. et al. Simultaneous multiple-emitter fitting for single molecule super-resolution imaging Simultaneous multiple-emitter fitting for single molecule super-resolution imaging. *Biomed. Opt. Express* **2,** 1377–1393 (2011).
90. Lee, J. *et al.* The nanoscale spatial organization of B-cell receptors on immunoglobulin M– and G–expressing human B-cells. *Mol. Biol. Cell* **28,** 511–523 (2017).

91. Bar-On, Dana; Wolter, S. et al. Super-resolution Imaging Reveals the Internal Architecture of Nano-sized Syntaxin Clusters. *J. Biol. Chem.* **287,** 27158–27167 (2012).
92. Ganguly, A. *et al.* A dynamic formin-dependent deep F-actin network in axons. *J. Cell Biol.* **210,** 401–417 (2015).
93. Xu, K., Babcock, H. P. & Zhuang, X. Dual-objective STORM reveals three-dimensional filament organization in the actin cytoskeleton. *Nat. Methods* **9,** 185–188 (2012).
94. Ester, M., Kriegel, H.-P., Xu, X. & Sander, J. A Density-Based Algorithm for Discovering Clusters in Large Spatial Databases with Noise. *KDD'96 Proc. Second Int. Conf. Knowl. Discov. Data Min.* 226–231 (1996).
95. Uruno, Takehito; Liu, J. et al. Activation of Arp2/3 complex- mediated actin polymerization by cortactin. *Nat. Cell Biol.* **3,** 259–266 (2001).
96. Weaver, A. M. *et al.* Cortactin promotes and stabilizes Arp2 / 3-induced actin filament network formation. *Curr. Biol.* **11,** 370–374 (2001).
97. Vardarajan, B. N. *et al.* Rare Coding Mutations Identified by Sequencing of Alzheimer Disease Genome-Wide Association Studies Loci. *ANN NEUROL* **78,** 487–498 (2015).
98. Levet, F. *et al.* SR-Tesseler : A method to segment and quantify localization-based super-resolution microscopy data. *Nat. Methods.* **12,** 1065-1071 (2015).
99. Andronov, L., Orlov, I., Lutz, Y. & Vonesch, J. ClusterViSu , a method for clustering of protein complexes by Voronoi tessellation in super- resolution microscopy. *Sci. Rep.* **6,** 1–9 (2016).
100. Gustafsson, N. *et al.* Fast live-cell conventional fluorophore nanoscopy with ImageJ through super-resolution radial fluctuations. *Nat. Commun.* **7,** 1–9 (2016).
101. Raiborg, C. *et al.* FYVE and coiled-coil domains determine the specific localisation of Hrs to early endosomes. *J. Cell Sci.* **114,** 2255–2263 (2001).
102. Raiborg, C., Bache, K. G., Mehlum, A., Stang, E. & Stenmark, H. Hrs recruits clathrin to early endosomes. *EMBO J.* **20,** 5008–5021 (2001).
103. Bache, K. G., Brech, A., Mehlum, A. & Stenmark, H. Hrs regulates multivesicular body formation via ESCRT recruitment to endosomes. *J. Cell Biol.* **162,** 435–442 (2002).
104. Baddeley, A., Rubak, E. & Turner, R. *Spatial Point Patterns: Methodology and Applications with R*. (Chapman and Hall/CRC Press, 2015).

Appendix A: Reagents, Antibodies and Solutions

PFA/PEM solution

A stock solution of 50 ml was prepared. PFA (Sigma-Aldrich) obtained from a stock powder form was diluted to a solution of 16 % (v/v). This one was then diluted into a concentration of 4 % PFA in cytoskeleton preserving buffer (PEM) solution composed of 80 mM at p.H 6.8 of PIPES (Sigma-Aldrich), 5mM EGTA (Sigma-Aldrich) and 2 mM $MgCl_2$ (Sigma-Aldrich) 12.5 ml of PFA 16 % (v/v) were added to 37.5 ml of PEM solution.

Imaging Buffer intermediate solutions

- DBuffer: Composed by 50 mM Tris and 10 mM NaCl.
- Catalase Solution: Catalase was diluted in deionized water to a concentration of 20 mg ml^{-1}.
- Oxygen scavenger (Stored up to 2 weeks):
  1. Dissolving 7 mg of Glucose Oxidase in 100 µl of DBuffer.
  2. Vortex to mix.
  3. Add 25 µl of Catalase Solution to Glucose Oxidase Solution.
  4. Centrifuge at maximum speed for 1 minute.
  5. Precipitate may be visible at the end of the tube. Use the yellow supernatant.
- MEA: Diluting Cysteamine in Hydrochloric Acid at 360 mM to a concentration of 77 mg ml^{-1}.

Table A.1 - Imaging Medium Reagents.

Reagent	Purity	Company
Glucose Oxidase from Aspergillus niger, Type VII	-	Sigma-Aldrich ™
Cyclooctatetraene	98 %	Sigma-Aldrich ™
Catalase from bovine liver	-	Sigma-Aldrich ™
Cysteamine	98 %	Sigma-Aldrich ™
Hydrochloric Acid	37 %-	Sigma-Aldrich ™

Table A.2 - Antibodies and probes.

Primary Antibody	Dilution	Company
EEA1	1:250	Santa Cruz Biotechnology
LAMP1	1:250	BD Biosciences
Secondary Antibody	**Dilution**	**Company**
Alexa-555 anti-Goat	1:250	Invitrogen
Alexa-555 anti-Rat	1:250	Life Technologies
Probe	**Dilution**	**Company**
Phalloidin-647	1:100	Life Technologies

Appendix B: Image Processing

Endosomal and Actin ROIs

For actin, the ROIs were selected as being the areas in the perinuclear region that include all or the greatest and more important parts of the perinuclear F-actin puncta. After evaluating in several cells for the same experiences, an area for this ROI was fixed for all cells. When testing actin correlations with early/late endosomes the actin ROI was fixed to a 5 µm × 5 µm square. For endosomal presence in the perinuclear region measurements the actin ROI was enlarged by 2.5 µm, resulting in an endosomal ROI of 10 µm × 10 µm. For all the experiences regarding actin and CD2AP the actin ROI was fixed to a square of 6.4 µm x 6.4 µm.

Endosomes

While F-actin images are obtained through dSTORM, endosome images are obtained from an epifluorescence snap. This implies a different kind of post-process. The objective is to have endosomes segmented the best way possible in order to create a binary mask of them and be able to introduce them in R to allow the possibility of analysis between the endosome patterns and the F-actin patterns. That being said, the epifluorescence image in the ROI (Figure B.1 a) starts by being filtered by a bandpass filter that highlights the bright spots corresponding to endosomes (Figure B.1 b). After, the highlighted signal is thresholded using the default threshold in FIJI (Figure B.1 c). After being thresholded, the mask (Figure B.1 d) is converted to individual dots so that it could be interpreted as a spatial point pattern in R.

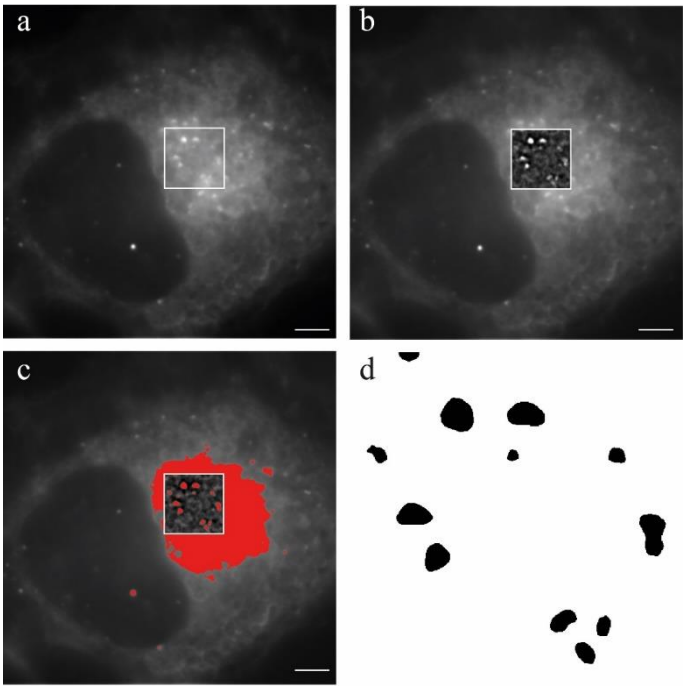

Figure B.1 - Endosomal segmentation protocol.

Appendix C: DBSCAN Working Principle and Parameter Determination

DBSCAN identifies clusters in large datasets of points by a propagative method that links points belonging to a common cluster based on two parameters; ε, the search radius and K, the minimum number of neighbors. These two criteria define whether a point belongs to a cluster or not. If a point has at least K neighbors within a radius ε or if a point is a neighbor of a point belonging to a cluster, this point is assigned to the cluster. The unassigned points are assigned to noise [94]. Our empirical protocol is described in the following **Figure C.2**.

In our experiments we found that the best combination of parameters was: A) ε = 66 nm, K = 30 **section 3.3**. B) ε = 60 nm, K= 30 for **sections 3.4 and 3.5**.

The following code determines the K parameter for clusters. After having the uncertainty distribution, **Figure C.2 a**, several K parameters are tested and their score is saved. Then, an overall plot as a function of K parameter gives us the best one, **Figure C.2 f**. The best K is the one that has the higher number of localizations of F-actin clusters identified in **Figure C.2 d** within identified clusters with that K. To check if the localizations are inside, an ellipse is computed around each cluster and the localizations are tested to see whether they are inside or outside the ellipse.

```
# DBSCAN K parameter determination

ell <- list()
Elipses <- list()

for (i in 1:length(All.SiCntrl$Actina)){
  for (j in 1: max(unique(ClustersSiCntrl30[[i]]$cluster))){
    if (max(unique(ClustersSiCntrl30[[i]]$cluster)) != 0){
      t <- subset(DataClustersSiCntrl[[i]], ClustersSiCntrl30[[i]]$cluster==j) # takes one cluster at the time.
      ell[[j]] <- dataEllipse(t$All.SiCntrl.Actina..j.....x..., +
                              t$All.SiCntrl.Actina..j.....y..., levels = 0.95, draw = FALSE) # fits ellipse to cluster.
    } else {
      j = 1
      ell[[j]] <- dataEllipse(c(-1,0,1,0), c(0,1,0,-1), levels = 0.95, draw = FALSE)
    }
  }
  Elipses[[i]] <- ell
  ell <- list()
}
q <- list()
Resultados <- list()

ElipsesSiCntrl30 <- Elipses

for (k in 1:length(Elipses)){
  for (w in 1:length(Elipses[[k]])){
    q[[w]] <- point.in.polygon(All.SiCntrl$Cluster.CM[[k]]$X*14.1/1000, +
                               All.SiCntrl$Cluster.CM[[k]]$Y*14.1/1000, Elipses[[k]][[w]][,1], Elipses[[k]][[w]][,2])
    Resultados[[k]] <- q # checks if fitted ellipses have the localization of putative clusters inside.
  }
  q <- list()
}
PontosDentro <- vector()
CentrosdeMassa <- vector()
FalsosPositivos <- vector()
PontosFora <- vector()
for (i in 1:length(Resultados)){ # Scores K parameter.
  PontosDentro[i] <- sum(sapply(Resultados[[i]],sum))
  CentrosdeMassa[i] <- length(All.SiCntrl$Cluster.CM[[i]][,1])
  FalsosPositivos[i] <- max(unique(ClustersSiCntrl30[[i]]$cluster)) - length(All.SiCntrl$Cluster.CM[[i]][,1])
  PontosFora[i] <- CentrosdeMassa[i] - PontosDentro[i]
}
ScoreSiCntrl30 <- list(PontosDentro = PontosDentro, CentrosdeMassa = CentrosdeMassa, + # Saves K parameter score.
                       FalsosPositivos = FalsosPositivos, PontosFora = PontosFora)
```

Figure C.1 - K parameter determination.

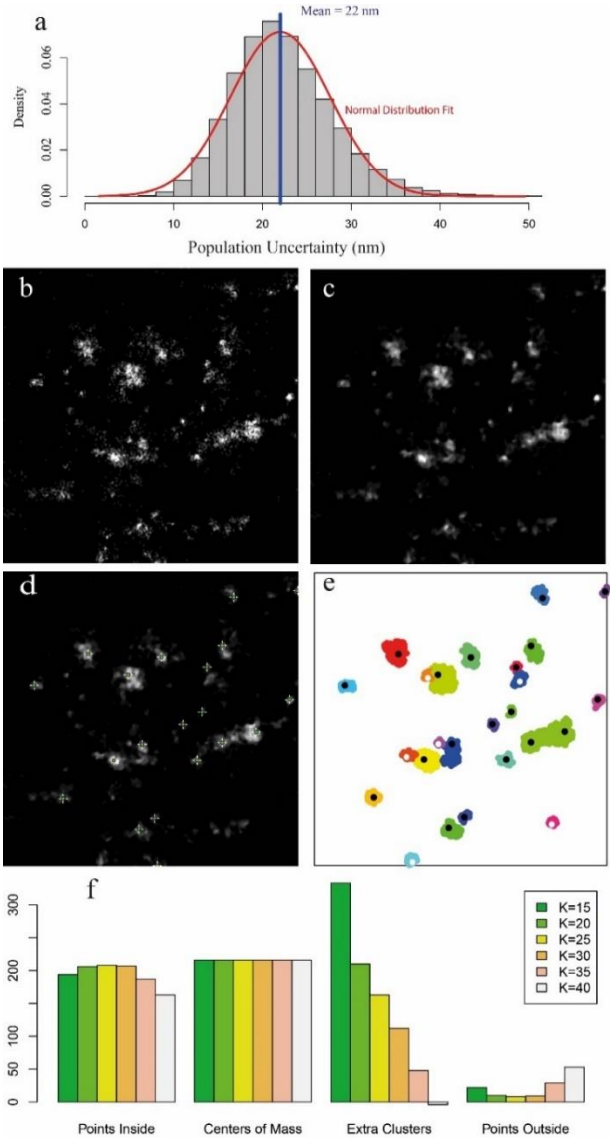

Figure C.2 - DBSCAN input parameters determination protocol.. **a)** ε determination. For every experience all localization uncertainties are merged and the population mean value (μ) serves as reference to calculate ε as ε = 3μ. Once that parameter has been fixed, we determine the minimum number of neighbor (K). The super resolution image is taken as reference **(b)**, a median filter is applied to reduce noise **(c)** and the identification of putative clusters is done by finding intensity local maximums **(d)**. Each local maxima is recorded as a coordinate. A swipe through several K parameters with fixed ε is performed in R, each one giving a certain score. **e)** Representation of identified clusters for a given K. Black dots represent localizations from d) that were within an identified cluster. White dots represent clusters not identified in d) but identified with DBSCAN. **f)** Score plot. Points inside represents the black dots inside a cluster determined by DBSCAN. Centers of mass represents putative clusters identified in the d) step. Extra clusters represent white dots in e) (Points that were not identified in d) but fulfill the density requirements of clusters. Points Outside represent putative clusters identified in d) that are not inside a cluster determined by DBSCAN. The K parameter chosen is the one with more point inside. Protocol adapted from [91].

Appendix D: Source Code

F-Actin Pattern Analysis

After all processing steps for actin, the list of resulting molecules is fed into R studio. In every analysis the points were transformed in a spatial point pattern using the RStudio package *Spatstat* [104]. This package requires both *X* and *Y* coordinates of the points as well a window which defines the limits of the pattern (ROI). After this, a home maid script was elaborated to characterize the correlations between both patterns. This procedure is divided in two main parts: Data Introduction and Pattern Analysis. A list is a basic structure in R that could contain different kinds of objects. A hyperframe is a structure of *Spatstat* that contains several lists. The following examples refer to **section 3.4** but the calculations for the other sections are adaptations.

Data Introduction

In this step we introduce the putative cluster localizations (***Cluster.CM.SiCntrl.3***), the F-actin detections (***SiCntrl.Actina.3***), Endosomes (***SiCntrl.Endossomas.3***), the ROI limits (***ROI***), meaning the limits of the point pattern. The F-actin detections and the endosomes together with the ROI limits form an object of class ppp (planar point pattern), (***PPPSiCntrl.Actina.3***) and (***PPPSiCntrl.Endossomas.3***).

```
# Retrieves data for analysis

# SiCntrl #
Cluster.CM.SiCntrl.3 <- read.table("Clusters CM.xls", header = TRUE) # reads xls file with Putative Cluster results
SiCntrl.Actina.3 <- read.table('resultados TS 647 merged 10000.xls', header=TRUE) # reads xls file with dSTORM localizations
SiCntrl.Endossomas.3 <- read.table('pontos endossomas.xls', header=TRUE) # # reads xls files with endosome points
ROI <- read.table('ROI.txt', header=TRUE) # reads txt file with ROI parameters.
SiCntrl.ROI.3 <- owin(c(ROI$Xcoord, ROI$Xcoord+ROI$width), +
                      c(ROI$Ycoord, ROI$Ycoord+ROI$height), unitname = "micro") # Creates Spatstat window.

PPPSiCntrl.Actina.3 <- ppp(SiCntrl.Actina.3$x..nm./1000, SiCntrl.Actina.3$y..nm./1000, SiCntrl.ROI.3) # Creats Point Pattern for actin
PPPSiCntrl.Actina.3 <- unique(PPPSiCntrl.Actina.3) # Ensures no repeated points, problematic for Spatstat routines
PPPSiCntrl.Actina.3 <- as.ppp(PPPSiCntrl.Actina.3) # Removes eventual points outside the window, coming from pixel errors.
#If existing is a very small percentage.

PPPSiCntrl.Endossomas.3 <- ppp(SiCntrl.Endossomas.3$XM, SiCntrl.Endossomas.3$YM, SiCntrl.ROI.3) # Creates Points Pattern for endosomes.

Lista.SiCntrl.Actina <- anylist(PPPSiCntrl.Actina.1,PPPSiCntrl.Actina.2,PPPSiCntrl.Actina.3) # Creates list with Actin Point Patterns
Lista.SiCntrl.Endossomas <- anylist(PPPSiCntrl.Endossomas.1,PPPSiCntrl.Endossomas.2,PPPSiCntrl.Endossomas.3) # Creates list with Endosome Point Patterns
Lista.SiCntrl.ROIS <- c(1,2,3) # Auxiliary link to the original files.
Lista.Clusters.CM <- anylist(Cluster.CM.SiCntrl.1,Cluster.CM.SiCntrl.2,Cluster.CM.SiCntrl.3) # Creates list with Putative Cluster results

All.SiCntrl <- hyperframe(ROIS = Lista.SiCntrl.ROIS, Actina = Lista.SiCntrl.Actina, +
                          Cluster.CM = Lista.Clusters.CM, Endossomas = Lista.SiCntrl.Endossomas) # Creates an Hyperframe (Array with several types of data)

# SiCD2AP # # Same Structure as in Control #
Cluster.CM.SiCD2AP.9 <- read.table("Clusters CM.xls", header = TRUE)
SiCD2AP.Actina.9 <- read.table('resultados TS 647 merged 10000.xls', header=TRUE)
SiCd2AP.Endossomas.9 <- read.table('pontos endossomas.xls', header=TRUE)
ROI <- read.table('ROI.txt', header=TRUE)
SiCD2AP.ROI.9 <- owin(c(ROI$Xcoord, ROI$Xcoord+ROI$width), c(ROI$Ycoord, ROI$Ycoord+ROI$height), unitname = "micro")

PPPSiCD2AP.Actina.9 <- ppp(SiCD2AP.Actina.9$x..nm./1000, SiCD2AP.Actina.9$y..nm./1000, SiCD2AP.ROI.9)
PPPSiCD2AP.Actina.9 <- unique(PPPSiCD2AP.Actina.9)
PPPSiCD2AP.Actina.9 <- as.ppp(PPPSiCD2AP.Actina.9)

PPPSiCd2AP.Endossomas.9 <- ppp(SiCd2AP.Endossomas.9$XM, SiCd2AP.Endossomas.9$YM, SiCD2AP.ROI.9)


Lista.SiCD2AP.Actina <- anylist(PPPSiCD2AP.Actina.2,PPPSiCD2AP.Actina.3,PPPSiCD2AP.Actina.9)
Lista.SiCD2AP.Endossomas <- anylist(PPPSiCd2AP.Endossomas.2,PPPSiCd2AP.Endossomas.3,PPPSiCd2AP.Endossomas.9)
Lista.SiCD2AP.ROIS <- c(2,3,9)
Lista.SiCD2AP.Clusters.CM <- anylist(Cluster.CM.SiCD2AP.2,Cluster.CM.SiCD2AP.3,Cluster.CM.SiCD2AP.9)

All.SiC2AP <- hyperframe(ROIS = Lista.SiCD2AP.ROIS, Actina = Lista.SiCD2AP.Actina, Clusters.CM = Lista.SiCD2AP.Clusters.CM, Endossomas = Lista.SiCD2AP.Endossomas)
```

Figure D.1 - Data Introduction

Pattern Analysis

Number of Detections

Takes the hyperframe created ***All.SiCntrl*** or ***All.SiC2AP*** and counts the number of points in the object of class ppp ***Actina***.

```
### Detections per Conditions ###

Npoints.SiCntrl <- with(All.SiCntrl, npoints(Actina)) # Returns a vector with Number of Detections for Control Conditions

Npoints.SiCd2AP <- with(All.SiC2AP, npoints(Actina))  # Same for siCD2AP cells.
```

Figure D.2 – Number of Detections.

Nearest Neighbor (NN)

Takes each pattern present in the hyperframe ***All.SiCntrl***, measures the nearest neighbor distance and saves the results as a percentage of the overall F-actin pattern each 5 nm from 0 nm to 100 nm (***NNdist.Control***). Each ROI is saved in the list ***All.NNdist.Control***.

```
### Nearest Neighbor measurement ###

All.NNdist.Control <- list()
NNdist.Control <- c()

# Goes through Hyperframes and for each pattern composes the comulative nearest neighbor measurements with user input for the intervals.
# Output is a list with a measurement for each pattern.

for (i in 1:length(All.SiCntrl$Actina)){

  NNdist.Control <- c()

  for (j in 1:length(seq(0,0.1,0.005))) {   # from 0 to 100 nm with 5 nm interval.

    NNdist.Control[j] <- npoints(subset(All.SiCntrl$Actina[[i]], nndist(All.SiCntrl$Actina[[i]])< seq(0,0.1,0.005)[j]))/ npoints(All.SiCntrl$Actina[[i]])
    # Saves Nearest Neighbor Measurement for this ROI.
  }
  All.NNdist.Control[[i]] <- NNdist.Control  # List with every measurement. Each entry is one ROI
}

#Same structure of Control
All.NNdist.SiCD2AP <- list()
NNdist.SiCD2AP <- c()

for (i in 1:length(All.SiC2AP$Actina)){

  NNdist.SiCD2AP <- c()

  for (j in 1:length(seq(0,0.1,0.005))){

    NNdist.SiCD2AP[j] <- npoints(subset(All.SiC2AP$Actina[[i]], nndist(All.SiC2AP$Actina[[i]])< seq(0,0.1,0.005)[j]))/ npoints(All.SiC2AP$Actina[[i]])

  }
  All.NNdist.SiCD2AP[[i]] <- NNdist.SiCD2AP

}
```

Figure D.3 - Nearest Neighbor.

Endosomal F-actin

In this step we calculated the percentage of F-actin that is inside the area of influence of each endosome. Since the endosome pattern comes has one pattern instead of being separated by endosome, we applied DBSCAN to identify each agglomerate of points has being one endosome (***EndossomasSiCntrl***). Besides that we also included the center of mass and the endosome radius for each endosome (***CMsEndossomasSiCNtrl***).

```
### Endosome identification with DBSCAN ###
##### SiCNtrl #####

DataEndossomasSiCntrl <- list()
EndossomasSiCntrl <- list()
All.SiCntrl2.1 <- All.SiCntrl2
CMsEndossomasSiCNtrl <- list()

### Each endosome can be seen as an island and therefore identified with DBSCAN.
### Creates a matrix with as many endosomes in the pattern with X and Y position its center of mass as well as its radius
### (maximum distance between center of mass and a composing point)
### The list CMsEndossomasSiCNtrl saves all measurements for all ROIS.


for (i in 1:length(All.SiCntrl2$Endossomas)){
  DataEndossomasSiCntrl[[i]] <- data.frame(All.SiCntrl2$Endossomas[[i]]$x, All.SiCntrl2$Endossomas[[i]]$y)
  EndossomasSiCntrl[[i]] <- dbscan(DataEndossomasSiCntrl[[i]], 0.1,10)  # identifies each endosome with DBSCAN.
  marks(All.SiCntrl2.1$Endossomas[[i]]) <- EndossomasSiCntrl[[i]]$cluster # marks each endosome
  Mat <- matrix(nrow = max(unique(marks(All.SiCntrl2.1$Endossomas[[i]]))), ncol = 3, +
          dimnames = list(c(1:max(unique(marks(All.SiCntrl2.1$Endossomas[[i]])))), c("XM", "YM", "Raio")))
  # Creates Matrix with Center of mass and radius for each one.
  for (j in 1:max(unique(marks(All.SiCntrl2.1$Endossomas[[i]])))){
    Endo <- subset(All.SiCntrl2.1$Endossomas[[i]], marks(All.SiCntrl2.1$Endossomas[[i]]) == j) # takes one endosome
    Mat[j,] <- c(mean(Endo$x), mean(Endo$y), max(nncross(Endo, ppp(mean(Endo$x), mean(Endo$y), Endo$window), what = "dist")))
    # fills the matrix with center of mass and r.
  }
  CMsEndossomasSiCNtrl[[i]] <- Mat
}
```

Figure D.4 - Endosome identification.

After having these information about endosomes we can measure F-actin quantities for endosome.

1. We measure the minimum distance of each F-actin point to an endosome (***first column ActinaEndossoma***).
2. We save the number of the endosomal point (***EndossomePoint***).
3. We transform that endosomal point in a number of endosome (***Endossoma***).
4. We subset actin per endosome (***Actina***) and find the number of points and percentages (***ActinAbs.Thresh*** and ***ActinPercent.Thresh***). Thresh means it depends of the endosomal radius.

```
ActinaEndossoma[[i]] <- nncross(All.SiCntrl2.1$Actina[[i]], All.SiCntrl2.1$Endossomas[[i]]) # Every actin point has nearest distance to an endosome.
NActina <- nrow(ActinaEndossoma[[i]]) # How many actin points
EndossomePoint <- ActinaEndossoma[[i]]$which # Takes endosome point with minimum distance to actin point.
QueEndossoma <- marks(All.SiCntrl2.1$Endossomas[[i]]) # Takes marks from endosomes.
Endossoma <- QueEndossoma[EndossomePoint] # Transforms endosome point into endosome number that belongs.
ActinaEndossoma[[i]]$Endossoma <- Endossoma # Adds this information to ActinaEndossoma matrix.
ActinaEndossoma[[i]]$Cluster <- All.SiCntrl2.1$Actina[[i]]$marks # Also adds information about cluster.
for (j in 1:max(unique(ActinaEndossoma[[i]]$Endossoma))){
  Actina <- subset(ActinaEndossoma[[i]], ActinaEndossoma[[i]]$Endossoma==j) # Works only with actin pattern belonging to endosome j
  Endossome[j] <- j
  ActinPercent.No.Tresh[j] <- nrow(Actina)/NActina
  Median.Distance.No.Tresh[j] <- median(Actina$dist)
  Has.Clusters[j] <- any(Actina$Cluster!=0)
  if (Has.Clusters[j] !=0){
    Which <- c(unique(Actina$Cluster[(Actina$Cluster !=0)]))
    Which.Clusters[[j]] <- as.numeric(Which)
    for (k in 1:length(Which)){
      Clust <- subset(Actina, Actina$Cluster==Which[k])
      Clust.Dist[k] <- min(Clust$dist)
      Distance.To.Endossome[[j]] <- Clust.Dist
      if (any(Clust$dist < 0.02)) {
        Clust.Coloc[k] <- 1
        Colocalize[[j]] <- Clust.Coloc
      } else {
        Clust.Coloc[k] <- 0
        Colocalize[[j]] <- Clust.Coloc
      }
    }
  } else {
    Which.Clusters[[j]] <- NaN
    Distance.To.Endossome[[j]] <- NaN
    Colocalize[[j]] <- NaN
  }
  ActinPercent.Tresh[j] <- nrow(subset(Actina, Actina$dist < CMsEndossomasSiCNtrl[[i]][j,3]))/NActina # Percentage of actin in area of influence
  ActinAbs.Tresh[j] <- nrow(subset(Actina, Actina$dist < CMsEndossomasSiCNtrl[[i]][j,3])) # Number of actin points in area of influence.
```

Figure D.5 - Endosomal F-actin.

Measuring Cluster Parameters

Following the protocol described in Appendix C we found that the best combination of input parameters to DBSCAN algorithm was ε = 60 nm and K = 30. The resulting clusters were assumed to have a decreasing density towards the cluster boundaries. We plotted a 95 % confidence ellipse from the data points and points falling outside this ellipse were removed from the cluster. We measured the number of clusters (***ClustersCMSSiCntrlAll***), the points per cluster (***first column ClusterStatsSiCntrl***) and fraction clustered (***FractionClusteredSiCntrl***).

```
# Calculates several cluster parameters.

ClustersCMSiCntrlAll <- list()
ClusterStatsSiCntrl <- list()
FractionClusteredSiCntrl <- c()
for (i in 1:length(All.SiCntrl$Actina)){
  Rows <- max(unique(ClustersSiCntrl30[[i]]$cluster))
  MAT <- matrix(nrow = Rows, ncol = 6, dimnames = list(c(1:Rows),c("ClusterPoints", "ClusterArea", "ClusterRatio","XM","YM","ROI")))
  ClustersCMSiCntrl <- list()
  for (j in 1:Rows){ # goes through every cluster.
    t <- subset(DataClustersSiCntrl[[i]], ClustersSiCntrl30[[i]]$cluster==j)
    t <- data.frame(t)
    PCA <- prcomp(t, center = TRUE)
    Elipse <- dataEllipse(PCA$x, levels = 0.95, draw = FALSE) # plots 95  confidence ellipse
    CheckPoints <- point.in.polygon(PCA$x[,1],PCA$x[,2], Elipse[,1],Elipse[,2]) # checks if the point is inside or not
    if (any(CheckPoints==0)){
      ZeroPos <- which(CheckPoints==0)
      ToZero <- as.numeric(rownames(t[ZeroPos,]))
      PCA$x <- PCA$x[-c(ZeroPos),] # removes points falling outside.
      t <- t[-c(ZeroPos),]
      ClustersSiCntrl30[[i]]$cluster[ToZero] <- 0
    }
    ClusterPoints <- length(PCA$x[,1])
    ClusterArea <- max(Elipse[,1])*max(Elipse[,2])*pi
    ClusterCM <- c(mean(t[,1]), mean(t[,2]))
    Axislength <- c(abs(max(Elipse[,1])), abs(max(Elipse[,2])))
    ClusterRatio <- min(Axislength)/max(Axislength)
    MAT[j,] <- c(ClusterPoints, ClusterArea, ClusterRatio, ClusterCM[1], ClusterCM[2], All.SiCntrl$ROIS[i])
    ClustersCMSiCntrl[[j]] <- ClusterCM
  }
  ClusterStatsSiCntrl[[i]] <- MAT
  ClustersCMSiCntrlAll[[i]] <- ppp(MAT[,4], MAT[,5], All.SiCntrl$Actina[[i]]$window)
  FractionClusteredSiCntrl[i] <- nrow(subset(DataClustersSiCntrl[[i]], ClustersSiCntrl30[[i]]$cluster>0))/ nrow(DataClustersSiCntrl[[i]])
}
```

Figure D.6 - Cluster Parameters.

Cluster Colocalization with Endosomes

To see if any cluster is colocalizing with an early endosome the script takes the actin that belongs to each endosome (***Actina***) and checks if there is any identified cluster in that subset. If there is any, its distance towards the endosome is measured and if it is less than 20 nm then there is colocalization. The result is saved in binary form in ***Colocalize***.

```
ActinaEndossoma[[i]] <- nncross(All.SiCntrl2.1$Actina[[i]], All.SiCntrl2.1$Endossomas[[i]]) # Every actin point has nearest distance to an endosome.
NActina <- nrow(ActinaEndossoma[[i]]) # How many actin points
EndossomePoint <- ActinaEndossoma[[i]]$which # Takes endosome point with minimum distance to actin point.
QueEndossoma <- marks(All.SiCntrl2.1$Endossomas[[i]]) # Takes marks from endosomes.
Endossoma <- QueEndossoma[EndossomePoint] # Transforms endosome point into endosome number that belongs.
ActinaEndossoma[[i]]$Endossoma <- Endossoma # Adds this information to ActinaEndossoma matrix.
ActinaEndossoma[[i]]$Cluster <- All.SiCntrl2.1$Actina[[i]]$marks # Also adds information about cluster.
for (j in 1:max(unique(ActinaEndossoma[[i]]$Endossoma))){
  Actina <- subset(ActinaEndossoma[[i]], ActinaEndossoma[[i]]$Endossoma==j) # Works only with actin pattern belonging to endosome j
  Endossome[j] <- j
  ActinPercent.No.Tresh[j] <- nrow(Actina)/NActina
  Median.Distance.No.Tresh[j] <- median(Actina$dist)
  Has.Clusters[j] <- any(Actina$Cluster!=0)
  if (Has.Clusters[j] !=0){
    which <- c(unique(Actina$Cluster[(Actina$Cluster !=0)]))
    Which.Clusters[[j]] <- as.numeric(which)
    for (k in 1:length(which)){
      Clust <- subset(Actina, Actina$Cluster==which[k])
      Clust.Dist[k] <- min(Clust$dist)
      Distance.To.Endossome[[j]] <- Clust.Dist
      if (any(Clust$dist < 0.02)) {
        Clust.Coloc[k] <- 1
        Colocalize[[j]] <- Clust.Coloc
      } else {
        Clust.Coloc[k] <- 0
        Colocalize[[j]] <- Clust.Coloc
      }
    }
  } else {
    Which.Clusters[[j]] <- NaN
    Distance.To.Endossome[[j]] <- NaN
    Colocalize[[j]] <- NaN
  }
```

Figure D.7 - Colocalization with Early Endosomes.

Appendix E: Summarized Results

Table E.1 - Summary of the results for CD2AP KD cells (Section 3.4) . Results are presented as average and standard error of the mean.

Condition	Number of Detections	Detections at 20 nm NN (%)	Number of Detections at Endosomes	Detections at Endosomes (%)
siCtrl	$(1.69 \pm 0.28) \times 10^4$	69.0 ± 3.4	$(3.98 \pm 0.54) \times 10^2$	34.6 ± 1.2
siCD2AP	$(6.07 \pm 0.92) \times 10^3$	52.7 ± 4.0	$(1.23 \pm 0.22) \times 10^2$	24.6 ± 7.1
Condition	**Number of Clusters**	**Fraction Clustered (%)**	**Detections Per Cluster**	**Cluster Colocalization with Endosomes (%)**
siCtrl	39.0 ± 7.0	29.1 ± 8.1	$(1.25 \pm 0.16) \times 10^2$	56.9 ± 7.2
siCD2AP	9.0 ± 2.0	8.8 ± 1.5	$(0.65 \pm 0.05) \times 10^2$	8.3 ± 8.3

Table E-2 - Summary of the results for Wild Type and Mutant CD2AP (Section 3.5) . Results are presented as average and standard error of the mean.

Condition	Number of Detections	Detections at 20 nm NN (%)	Number of Detections at Endosomes	Detections at Endosomes (%)
GFP	$(1.30 \pm 0.08) \times 10^4$	72.6 ± 3.0	$(4.09 \pm 0.42) \times 10^2$	49.7 ± 2.5
WT	$(7.15 \pm 0.40) \times 10^3$	67.1 ± 2.0	$(2.08 \pm 0.24) \times 10^2$	41.8 ± 4.6
MUT	$(6.93 \pm 1.60) \times 10^3$	61.7 ± 3.0	$(1.98 \pm 0.25) \times 10^2$	47.8 ± 6.0
Condition	**Number of Clusters**	**Fraction Clustered (%)**	**Detections Per Cluster**	**Cluster Colocalization with Endosomes (%)**
GFP	29.0 ± 2.0	34.9 ± 7.8	$(1.65 \pm 0.17) \times 10^2$	51.4 ± 11.8
WT	18.0 ± 2.0	24.6 ± 4.4	$(1.02 \pm 0.10) \times 10^2$	36.7 ± 7.6
MUT	14.0 ± 6.0	11.2 ± 3.7	$(0.72 \pm 0.08) \times 10^2$	24.9 ± 8.0